

LucidAtlas: Learning Uncertainty-Aware, Covariate-Disentangled, Individualized Atlas Representations

Yining Jiao¹ Sreekalyani Bhamidi¹ Huaizhi Qu¹ Carlton Zdanski¹ Julia Kimbell¹ Andrew Prince¹
Cameron Worden¹ Samuel Kirse¹ Christopher Rutter¹ Benjamin Shields¹ Jisan Mahmud¹ Tianlong Chen¹
Marc Niethammer²

¹UNC-Chapel Hill

²UCSD

Abstract

The goal of this work is to develop principled techniques to extract information from high dimensional data sets with complex dependencies in areas such as medicine that can provide insight into individual as well as population level variation. We develop *LucidAtlas*, an approach that can represent spatially varying information, and can capture the influence of covariates as well as population uncertainty. As a versatile atlas representation, *LucidAtlas* offers robust capabilities for covariate interpretation, individualized prediction, population trend analysis, and uncertainty estimation, with the flexibility to incorporate prior knowledge. Additionally, we discuss the trustworthiness and potential risks of neural additive models for analyzing dependent covariates and then introduce a marginalization approach to explain the dependence of an individual predictor on the models' response (the atlas). To validate our method, we demonstrate its generalizability on two medical datasets. Our findings underscore the critical role of by-construction interpretable models in advancing scientific discovery. Our code will be publicly available upon acceptance.

1 INTRODUCTION

In the context of medical image analysis and computational anatomy, an *atlas* is a standardized representation of biological structures that serves as a reference model [Joshi et al., 2004, Thompson and Toga, 2002]. An atlas is often created by aggregating data from multiple patients to represent "typical" or "average" anatomy. Atlases are crucial in medical research, diagnosis, and treatment planning, providing a baseline for comparison with individual patient data [Hong et al., 2013, Commowick et al., 2005]. Although

often representing average structures, some atlases also incorporate information on anatomical variability within a population [Jin et al., 2019, Kovačević et al., 2005].

The goal of this work is to enhance atlas representations by incorporating covariates and uncertainties, providing clinicians with a more comprehensive tool for disease analysis. Our approach goes beyond traditional models, offering covariate disentanglement and uncertainty estimation for improved population understanding. Specifically, accounting for covariates and capturing subject- and population-level aspects about the data is important to address the following questions relevant for clinicians and technical users who might want to build upon our model:

Covariate-Level ① *Covariate Disentanglement*. Understanding the effects of covariates is frequently a goal of medical studies. Therefore, it is critical to disentangle covariate effects on the population to interpret an atlas representation and to ensure that these effects align with human knowledge. Inherently interpretable models are desirable for atlas building because such atlas representations are then transparent by construction [Rudin, 2019]. ② *Covariate Marginalization*. Clinicians usually understand the importance of a covariate by analyzing its relationship with the response, e.g., how a population trend evolves under the control of a specific covariate regardless of the existence of other covariates. For example, how does a brain change for normal people versus Alzheimer patients, regardless of age? ③ *Prior Knowledge*. Suppose we have prior knowledge about some or all covariates, e.g., monotonicity¹ how can such prior knowledge assist in better atlas construction? Do our modeling assumptions align with our prior knowledge and are they reasonable for human data?

Subject-Level ① *Predictions based on the Population Trend*. Is the constructed atlas a good predictor for individual anatomies given their covariates? ② *Individualized*

¹For example, a pediatric airway should typically expand with age, as a child grows.

Temporal Analysis. Can the model provide individualized predictions at time B based on observations based on a prior time A ? This is a challenging task, as the collected data often consists of numerous one-time observations rather than longitudinal data.

Population-Level ① *Individual Variability.* Variation across the population may surpass the variation explained by covariates. How can we quantify population variation not captured by the covariates? ② *Heteroscedasticity.* Variability may be heteroskedastic across covariates and anatomical geometry. For example, population variance may differ change with age and airway location when constructing a pediatric airway atlas.

Spatial-Level ① *Spatial Dependence.* Capturing spatial dependence is essential for atlas construction. For instance, different anatomical locations may exhibit distinct population trends and variations influenced by covariates, highlighting the need to model spatial dependence effectively.

To address covariate-, subject-, population-, and spatial-questions simultaneously, we propose the versatile *LucidAtlas* model. This uncertainty-aware, covariate-disentangled individualized atlas representation extends the Neural Additive Model (NAM) [Agarwal et al., 2020] to enhance atlas construction by integrating uncertainty quantification and incorporating prior knowledge. We introduce a marginalization approach that incorporates covariate dependencies to provide a more comprehensive covariate interpretation; while NAM’s interpretations only focus on individual covariate effects in isolation.

The main contributions of *LucidAtlas* are as follows:

- 1) *LucidAtlas* is a versatile atlas representation capable of enhancing traditional atlas representations by incorporating covariates, uncertainties, and prior knowledge, providing clinicians with a more comprehensive tool for disease analysis.
- 2) We show potential risks when using NAMs for covariate interpretation in the context of dependent features. We further propose a marginalization approach to address these shortcomings.
- 3) We validate our approach on two medical datasets: 1) the OASIS Brain Volume dataset [Jack Jr et al., 2008], and 2) a Pediatric Airway Shape dataset. Our experiments quantitatively demonstrate the superior performance of *LucidAtlas* compared to baseline methods.

2 RELATED WORK

We first introduce the three most related research directions.

Method	Covariate-		Subject-	Population-	Spatial-
	Cov. Marg.	Prior.	Ind. Pred.	Hetero.+Aleatoric	Spa. Dep.
NAM [Agarwal et al., 2020]	✗	✗	✗	✗	✗
OAK [Lu et al., 2022]	✓	✗	✗	✗	✗
LA-NAM [Bouchiat et al., 2023]	✗	✗	✓	✗	✗
NAMLSS [Thielmann et al., 2024]	✗	✗	✓	✓	✗
NAISR [Jiao et al., 2023]	✗	✗	✓	✗	✓
<i>LucidAtlas</i> (Ours)	✓	✓	✓	✓	✓

Table 1: Comparison of interpretable representations based on the desirable properties discussed in Sec.1. **Cov.Marg.** denotes covariate marginalization. **Prior.** indicates prior knowledge. **Ind. Pred.** indicates individualized prediction, i.e., whether the model can predict a response for time B given an earlier observation at time A . **Hetero.+Aleatoric** indicates whether the model considers heteroscedasticity when modeling aleatoric uncertainty. **Spa. Dep.** indicates spatial dependence. A ✓ indicates that a model has a property; a ✗ indicates that it does not. Only *LucidAtlas* has all the desired properties.

Additive Models Model-agnostic methods, such as Partial Dependence [Friedman, 2001], SHAP [Lundberg, 2017], and LIME [Ribeiro et al., 2016], offer a standardized approach to explaining machine learning predictions. However, when applied to deep neural networks (DNNs), these methods may fail to provide faithful representations of their full complexity [Rudin, 2019]. A more transparent alternative involves leveraging Generalized Additive Models (GAMs) [Hastie, 2017], where the response variable y is modeled using an additive structure:

$$E[y|c_1, \dots, c_N] = h(\beta_0 + f_1(c_1) + \dots + f_N(c_N)) \quad (1)$$

where $h(\cdot)$ is the inverse of the link function (a form of activation function); β_0 denotes the intercept and $f_i(\cdot)$ represent independent functions for the i^{th} covariate. Neural Additive Models (NAMs) [Agarwal et al., 2020, Jiao et al., 2023] build upon this framework, offering enhanced interpretability while maintaining the flexibility of neural networks. Specifically, for NAMs the functions $f_i(\cdot)$ are deep neural networks. NAISR [Jiao et al., 2023] pioneers the use of NAMs to capture spatial deformations with respect to an estimated atlas shape that is modulated by covariates. *LucidAtlas* extends this concept by integrating NAMs to construct an atlas that captures population trends and uncertainties with spatial dependencies.

Epistemic Uncertainty versus Aleatoric Uncertainty

Estimating uncertainty is important to understand the quality of a model fit and to capture variations across the data population. Two different types of uncertainties need to be distinguished: epistemic uncertainty captures model uncertainty whereas aleatoric uncertainty captures uncertainty in the data [Hüllermeier and Waegeman, 2021].

More attention is generally paid to epistemic uncertainties in the context of interpretable models [Wang et al., 2025]. NAMs used ensembling to estimate model uncertainties [Agarwal et al., 2020]. LA-NAM used a Laplace approximation for uncertainty estimation [Bouchiat et al., 2023] with NAMs. In atlas construction, aleatoric uncertainty is especially important when individual differences

in a dataset are large. Capturing aleatoric uncertainty is crucial in medicine to understand population variations. NAMLSS [Thielmann et al., 2024] can model aleatoric uncertainty by using NAMs to approximate the parameters $\{\theta^{(n)}\}$ of a chosen data distribution [Thielmann et al., 2024], as

$$\theta^{(n)} = h^{(n)} \left(\beta^{(n)} + \sum_{i=1}^N f_i^{(n)}(c_i) \right) \quad (2)$$

where $\theta^{(n)}$ can for example be the mean and variance of Gaussian distributions; $\beta^{(n)}$ denotes the parameter-specific intercept and $f_i^{(n)}$ represents the feature network for the n -th parameter for the i -th feature. *LucidAtlas* extends NAMLSS to a more versatile representation, enabling individualized prediction, incorporating prior knowledge, and capturing spatial dependencies.

Heteroscedasticity versus Homoscedasticity Distinguishing between homoscedasticity and heteroscedasticity is crucial in statistical analysis, especially for regression models. Homoscedasticity indicates constant variance of random variables, whereas heteroscedasticity indicates that the variance of random variables may differ [Wooldridge et al., 2016]. For example, when modeling airway cross-sectional area the population variance may change (increase) with age. *LucidAtlas* assumes and supports estimating heteroscedasticity with respect to different locations in an anatomical region and with respect to covariates across a patient population. Many interpretable approaches assume homoscedasticity, e.g., OAK-GP [Lu et al., 2022] and LA-NAM [Bouchiat et al., 2023] assume homoscedasticity in their additive networks. To our knowledge, only NAMLSS considers heteroscedasticity in its additive network design [Thielmann et al., 2024]. However, NAMLSS interprets individual covariate effects and uncertainties in isolation resulting, as we will see, in difficulties for data interpretation. *LucidAtlas* advances beyond NAMLSS by capturing spatial heteroscedasticity and incorporating covariate dependencies via a marginalized covariate interpretation approach.

Table 1 compares *LucidAtlas* to related interpretable models with respect to the discussed properties above. A more comprehensive discussion of related work is available in Sec. S.1 of the Supplementary Material.

3 METHOD

Sec. 3.1 introduces our general atlas construction formulation. Sec. 3.2 describes *LucidAtlas*, which by construction ensures *covariate disentanglement based on an additive model formulation*. Sec. 3.3 discusses the potential concerns for neural additive models when dealing with dependent covariates. To address these concerns Sec. 3.4 introduces our covariate marginalization approach. Table S.6 lists the mathematical notations used in this paper.

3.1 GENERAL ATLAS FORMULATION

Consider a set of anatomies $\{\mathcal{Y}^k\}$, where each anatomy \mathcal{Y}^k is associated with a vector of covariates $\mathbf{c}^k = [c_1^k, \dots, c_i^k, \dots, c_N^k]$. A point within an anatomy is denoted as x , with an observed value $y \in \mathbb{R}$, which is the primary focus of our study.

Our goal is to construct an atlas representation that addresses the questions outlined in Section 1 by learning the mapping from covariates \mathbf{c} and spatial location x to observations y , while simultaneously accounting for heteroscedastic uncertainties within the population, represented as $p(y | \mathbf{c}, x) = \mathcal{N}(f^m(\mathbf{c}, x), f^v(\mathbf{c}, x))$.

3.2 LUCIDATLAS FORMULATION

3.2.1 Introducing Spatial Dependency

We develop *LucidAtlas* based on NAMLSS [Thielmann et al., 2024], first extending it by incorporating spatial dependency, which is not explicitly modeled in NAMLSS. To achieve this, we introduce neural subnetworks $\{f_i(c_i, x)\}$ that predict the distributional parameters of $p(y | \mathbf{c}, x)$. Each network $f_i(c_i, x)$ has two outputs: $f_i^m(c_i, x)$ and $f_i^v(c_i, x)$, which capture the contribution from c_i at location x to the mean and variance of $p(y | \mathbf{c}, x)$ respectively. The overall population mean and variance are then obtained by summing these individual contributions:

$$f^m(\mathbf{c}, x) = \sum_{i=1}^N f_i^m(c_i, x), f^v(\mathbf{c}, x) = \sum_{i=1}^N f_i^v(c_i, x). \quad (3)$$

By explicitly modeling spatial dependencies, *LucidAtlas* extends NAMLSS to spatial atlas construction.

Loss Function. We optimize the subnetworks $\{f_i\}$ by minimizing the negative log-likelihood resulting in the loss function

$$\mathcal{L}(\{f_i\}, \mathbf{c}, x) = \frac{1}{2} \log(2\pi \cdot f^v(\mathbf{c}, x)) + \frac{(y - f^m(\mathbf{c}, x))^2}{2 \cdot f^v(\mathbf{c}, x)}, \quad (4)$$

where y is the observation at location x given the covariates \mathbf{c} .

3.2.2 Disentangled Covariate Effects

We choose NAMs [Agarwal et al., 2020, Thielmann et al., 2024] for atlas representation due to their inherent ability to disentangle covariate effects, enabled by their additive subnetwork design. The disentangled effect of covariate c_i on the population trend is represented by $f_i^m(c_i, x)$, while its contribution to the population variation is captured by $f_i^v(c_i, x)$.

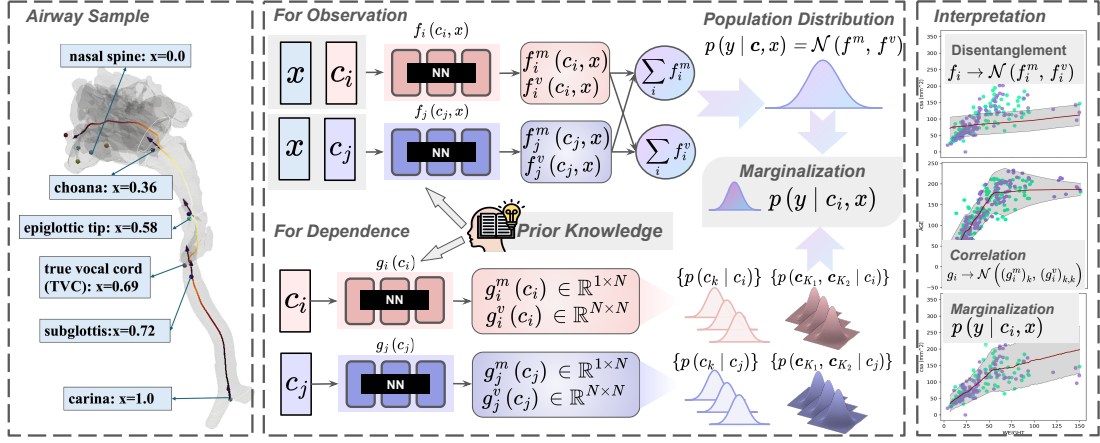


Figure 1: LucidAtlas: Learning an Uncertainty-Aware, Covariate-Disentangled, Individualized Atlas Representation. ① As an example use case, we depict an airway with its anatomical landmarks at different depths (i.e., anatomical location) along its centerline [Hong et al., 2013]. ② During training, each subnetwork $f_i(c_i, x)$ receives the location x and covariate c_i as input to predict the covariate-specific distributional parameters f_i^m and f_i^v , which are added to obtain the overall distributional parameters to capture the population trend and variation as $f^m = \sum_i f_i^m$ and $f^v = \sum_i f_i^v$ respectively. ③ The goal of marginalization is to discover $p(y|c_i, x)$, by integrating out the potentially dependent covariates $\{c_k\}_{k \neq i}$. Each subnetwork $g_i(c_i)$ receives covariate c_i to parameterize a multivariate Gaussian distribution $p(c|c_i)$ for all N covariates, from which we obtain $p(c_k|c_i)$ and $p(c_{K_1}, c_{K_2}|c_i)$. The marginalization requires that the outputs of $\{f_i\}$ and $\{g_i\}$ are as described in Sec. 3.4. ④ LucidAtlas can obtain different interpretations, i.e., 1) a covariate disentanglement corresponding to each covariate’s additive effect from $\{f_i\}$; 2) dependence between covariates modeled by $\{g_i\}$ as $p(c_k|c_i)$ and 3) a marginalization illustrating the overall impact from each covariate on the predicted response (here the cross-sectional area y at a specific location x) via marginalization. ⑤ Monotonic neural networks by construction are used if the influence of a covariate on the response is assumed to be monotonic based on prior knowledge/domain knowledge; otherwise, a multi-layer perceptron (MLP) is used to parameterize the subnetworks.

3.2.3 Prior Knowledge

To take a further step, we improve the uncertainty-aware neural additive model [Thielmann et al., 2024] by incorporating *prior knowledge* of monotonicity [Kitouni et al., 2023] for the covariates. Specifically, assuming that the distribution of the response y has a stochastically increasing relationship with respect to a particular covariate c_j (while keeping all other covariates fixed), can be incorporated via the modeling ansatz

$$\frac{\partial f^m(c, x)}{\partial c_j} = \sum_{i=1}^N \frac{\partial f_i^m(c_i, x)}{\partial c_j} = \frac{\partial f_j^m(c_j, x)}{\partial c_j} \geq 0. \quad (5)$$

As illustrated in Fig. 1, $f_j(c_j)$ can be parameterized using a monotonic Lipschitz neural network by design [Kitouni et al., 2023] when such prior monotonicity information is available. This design guarantees the monotonicity of $f_j(c_j)$ by construction and ensures that the interpretations derived from the NAMs align with human prior knowledge.

3.3 RETHINKING THE NEURAL ADDITIVE MODEL

The underlying assumption behind NAMs is that each covariate contributes independently to the outcome. Even if the covariates are dependent, the NAMs will spread out the contribution from each covariate to its subnetworks as ad-

ditive functions [Agarwal et al., 2020]. In most real-world applications, such as our airway atlas construction problem in Sec. 3.1, the independence between covariates cannot be guaranteed. A *natural question is whether accepting the independence assumption unquestioningly and directly using NAMs is appropriate*. In this section, we discuss trustworthiness and the potential risks of neural additive models.

We can investigate this problem with a toy example, where $y = \sin(c_1) + c_2 + \epsilon$ where ϵ is a noise term and c_1, c_2 are covariates that influence the observed outcome y . Assuming there is a NAM that already fits this function well, the subnetworks capture $f_1(c_1) = \sin(c_1)$ and $f_2(c_2) = c_2$ and thus approximate y with $f(c_1, c_2) = f_1(c_1) + f_2(c_2)$.

If we want to interpret the population trend of y only with respect to c_1 , we need to marginalize c_2 out as,

$$\begin{aligned} F_1(c_1) &= \int_{-\infty}^{\infty} [f_1(c_1) + f_2(c_2)] p(c_2|c_1) dc_2 \\ &= \underbrace{f_1(c_1)}_{\text{Interpretation from NAMs}} + \underbrace{\int_{-\infty}^{\infty} f_2(c_2) p(c_2|c_1) dc_2}_{\text{Interpretation from Dependence: } := h_1(c_1)} \end{aligned} \quad (6)$$

where $h_1(c_1)$ measures how the dependence between c_1 and c_2 influences the marginalization $F_1(c_1)$. We can see from Eq. (6) that $F_1(c_1)$ is composed of the interpretation from the NAM’s subnetwork plus the interpretation from the dependence between c_1 and c_2 as $h_1(c_1)$.

If c_1 and c_2 are **independent**, $h_1(c_1) = \int_{-\infty}^{\infty} f_2(c_2)p(c_2|c_1)dc_2 = \int_{-\infty}^{\infty} f_2(c_2)p(c_2)dc_2 = \text{constant}$, which means the marginalization is the actual covariate disentanglement in Eq. (3) plus a constant. If c_1 and c_2 are **dependent**, $h_1(c_1)$ is a function of c_1 which no longer needs to be a constant and could be a non-trivial function of c_1 arising from the inherent stochastic dependence between c_1 and c_2 . Therefore, considering the relationship between c_1 and c_2 is crucial when using either covariate by itself to interpret the population trend.

In summary, disentangled covariate effects of NAMs, combined with those effects contributed by covariate dependence, shape human-understandable explanations aligned with population trends. *While ignoring potential dependencies in NAMs may not impact prediction performance, it can result in ambiguous or misleading interpretations when analyzing population trends.* More analysis is available in Sec. S.2.2 in the Supplementary Material.

3.4 COVARIATE MARGINALIZATION

Due to space constraints, the full derivation is provided in Sec. S.2.3 of the Supplementary Material. This section introduces our proposed marginalization approach to improve the trustworthiness of NAMs when trying to understand the dependency of a covariate on the response. The dependency of covariates can be modeled with a multivariate Gaussian distribution as $p(\mathbf{c}|c_i) = \mathcal{N}(\hat{\boldsymbol{\mu}}(c_i), \hat{\boldsymbol{\Sigma}}(c_i))$ where $\hat{\boldsymbol{\mu}}(c_i)$ represents the mean vector and $\hat{\boldsymbol{\Sigma}}(c_i)$ the covariance matrix conditioned on c_i . From $p(\mathbf{c}|c_i)$, one can extract the distribution of an individual covariate c_k conditioned on c_i , as $p(c_k|c_i) = \mathcal{N}(\hat{\mu}_k(c_i), \hat{\Sigma}_{k,k}(c_i))$, e.g., how age c_i determines weight c_k . One can also extract the joint distribution of c_{K_1} and c_{K_2} conditioned on c_i as $p(c_{K_1}, c_{K_2}|c_i)$ from $p(\mathbf{c}|c_i)$, i.e.,

$$p(c_{K_1}, c_{K_2}|c_i) = \mathcal{N}\left(\begin{bmatrix} \hat{\mu}_{K_1}(c_i) \\ \hat{\mu}_{K_2}(c_i) \end{bmatrix}, \begin{bmatrix} \hat{\Sigma}_{K_1, K_1}(c_i) & \hat{\Sigma}_{K_1, K_2}(c_i) \\ \hat{\Sigma}_{K_2, K_1}(c_i) & \hat{\Sigma}_{K_2, K_2}(c_i) \end{bmatrix}\right), \quad (7)$$

where $\hat{\Sigma}_{K_1, K_2}(c_i)$ is the covariance between c_{K_1} and c_{K_2} .

We employ subnetworks $\{g_i(c_i)\}$, each controlled by an individual covariate c_i , to model the corresponding conditional distributions $\{p(\mathbf{c}|c_i)\}$. Specifically, each subnetwork $g_i(c_i)$ captures a multivariate Gaussian distribution, expressed as: $p(\mathbf{c}|c_i) = \mathcal{N}(g_i^m(c_i), g_i^v(c_i))$, where the mean vector $g_i^m(c_i)$ and the covariance matrix $g_i^v(c_i)$ are predicted by $g_i(c_i)$, as illustrated in Fig. 1.

Next, from Eq. (3), the observation y can be formulated as

$$y = f^m(\mathbf{c}, x) + f^v(\mathbf{c}, x) \cdot \epsilon, \quad \epsilon \sim \mathcal{N}(0, 1). \quad (8)$$

With trained $\{f_i\}$ and $\{g_i\}$, we now investigate how c_i influences the distribution of the observation y as $p(y|c_i, x) = \mathcal{N}(\tilde{\mu}(c_i, x), \tilde{\sigma}^2(c_i, x))$, where $\tilde{\mu}(c_i, x)$ is the expectation of y when fixing c_i and x , i.e. $E[y|c_i, x]$; and $\tilde{\sigma}^2(c_i, x)$ is the variance of y when fixing c_i and x , i.e. $\text{Var}(y|c_i, x)$.

Mean of $p(y|c_i, x)$. We expand the two variable case in Sec. 3.3 to multi-covariates, with the *law of total expectation* (1)

$$\begin{aligned} \tilde{\mu}(c_i, x) &= f_i^m(c_i, x) + \int_{-\infty}^{\infty} \left(\sum_{k \neq i} f_k^m(c_k, x) \right) p(\mathbf{c}_{k \neq i}|c_i) d\mathbf{c}_{k \neq i} \\ &= f_i^m(c_i, x) + \sum_{k \neq i} \int_{-\infty}^{\infty} f_k^m(c_k, x) p(c_k|c_i) dc_k, \end{aligned} \quad (9)$$

where $f_k^m(c_k)$ represents the interpretation from the additive subnetwork f_k of LucidAtlas and $\mathbf{c}_{k \neq i} = [c_1, \dots, c_{i-1}, c_{i+1}, \dots, c_N]$.

Eq. (9) indicates that even when multiple covariates are involved, only conditional dependencies with respect to individual covariates ($p(c_k|c_i)$) are required to compute $\tilde{\mu}(c_i, x)$ as a consequence of the additive model for a NAM, which simplifies computations.

Variance of $p(y|c_i, x)$. The *law of total variance* is $\text{Var}(Y) = E[\text{Var}(Y|X)] + \text{Var}(E[Y|X])$ which states that the total variance of a random variable Y can be broken into two parts: ① the **expected variance of Y given X** , which represents how much Y fluctuates around its mean for each specific value of X ; and ② The variance of the **expected value of Y given X** , which measures how much the mean of Y changes as X varies. With the *law of total variance*,

$$\text{Var}(y|c_i, x) = \underbrace{E[\text{Var}(y|\mathbf{c}_{k \neq i}, c_i, x)]}_{\text{①: } \tilde{\sigma}_E^2(c_i, x)} + \underbrace{\text{Var}(E[y|\mathbf{c}_{k \neq i}, c_i, x])}_{\text{②: } \tilde{\sigma}_V^2(c_i, x)} \quad (10)$$

The expected variance of $f^v(\mathbf{c}, x)$ given c_i and x is

$$\tilde{\sigma}_E^2(c_i, x) = f_i^v(c_i, x) + \sum_{k \neq i} \int_{-\infty}^{\infty} f_k^v(c_k, x) p(c_k|c_i) dc_k. \quad (11)$$

And the variance of the expected value of $f^m(\mathbf{c}, x)$ given c_i and x can be computed as

$$\begin{aligned} \tilde{\sigma}_V^2(c_i, x) &= \text{Var}(E[y|\mathbf{c}_{k \neq i}, c_i, x]) = \text{Var}\left(\sum_{k \neq i} f_k^m(c_k, x)|c_i, x\right) \\ &= \sum_{k \neq i} \underbrace{\text{Var}(f_k^m(c_k, x)|c_i, x)}_{\text{③}} + \sum_{K_1 \neq K_2 \neq i} \underbrace{\text{Cov}(f_{K_1}^m(c_{K_1}, x), f_{K_2}^m(c_{K_2}, x)|c_i, x)}_{\text{④}} \end{aligned} \quad (12)$$

where

$$\begin{aligned} \text{③} &= \int_{-\infty}^{\infty} (f_k^m(c_k, x) - \tilde{\mu}_k(c_i, x))^2 p(c_k|c_i) dc_k, \\ \tilde{\mu}_k(c_i, x) &= \int_{-\infty}^{\infty} f_k^m(c_k, x) p(c_k|c_i) dc_k \end{aligned} \quad (13)$$

$$\text{④} = \int_{-\infty}^{\infty} \int_{-\infty}^{\infty} f_{K_1}^m(c_{K_1}, x) f_{K_2}^m(c_{K_2}, x) p(c_{K_1}, c_{K_2}|c_i) dc_{K_1} dc_{K_2} - \tilde{\mu}_{K_1}(c_i, x) \tilde{\mu}_{K_2}(c_i, x) \quad (14)$$

Eqs. (11)-(14) imply that instead of sampling the entire covariate space, one only needs to sample from the joint Gaussian distribution between the two covariates, conditioned on the individual covariates, to obtain the marginalized distribution $p(y|c_i, x)$.

Approximation. The integrals in $\tilde{\mu}(c_i, x)$ (in Eq. (9)), $\tilde{\sigma}_E^2(c_i, x)$ (in Eq. (11)) and $\tilde{\sigma}_V^2(c_i, x)$ (in Eqs. (11)-(14)) can be approximated using Monte Carlo sampling from $p(c_k|c_i)$ and $p(c_{K_1}, c_{K_2}|c_i)$.

Computational Complexity. Suppose there are N covariates and L samples. The computational complexity of marginalizing the NAM for a covariate is $\mathcal{O}(LN)$, making it feasible in practice. In contrast, for a black-box model, which does not assume our additive structure, the complexity is exponentially higher at $\mathcal{O}(L^N)$, making direct computation infeasible for large N .

As a result, we obtain $\tilde{\mu}(c_i, x)$ and $\tilde{\sigma}^2(c_i, x) = \tilde{\sigma}_E^2(c_i, x) + \tilde{\sigma}_V^2(c_i, x)$ to parameterize $p(y|c_i) = \mathcal{N}(\tilde{\mu}(c_i, x), \tilde{\sigma}^2(c_i, x))$, capturing the influence of a single covariate c_i on the observation y . Our approach aligns with NAM interpretations and can be applied post-hoc.

3.4.1 Imputation

Our approach naturally facilitates the imputation of missing covariates, as it inherently predicts the conditional distributions $\{p(c_k | c_i)\}$, enabling a principled way to estimate missing values. Specifically, if c_i is missing, one can choose the g_s whose uncertainty is the smallest as the predictor for c_i as $s \leftarrow \arg \min_{k, k \neq i} \{g_{k,i}^v(c_k)\}$.

3.4.2 Individualized Prediction

One challenge in the context of atlas discovery is to make individualized predictions when observations are predominantly limited to a single time point, i.e., when the atlas is built from cross sectional data. *LucidAtlas* provides an approach for individualized prediction based on previous observations. Note that this approach is not based on true longitudinal data (as such data is frequently not available) but instead aims to predict individual future responses based on the cross-sectional population trend.

We define our problem as follows. Given an observation y^t at x with its corresponding covariates \mathbf{c}^t at time t , how will a subject's response change when \mathbf{c}^t changes to \mathbf{c}^{t+1} at time $t + 1$? First, we can obtain the probability distribution with *LucidAtlas*, as $p(y^t|\mathbf{c}^t, x) = \frac{1}{\sqrt{2\pi f^v(\mathbf{c}^t, x)}} \exp(-\frac{(y^t - f^m(\mathbf{c}^t, x))^2}{2 \cdot f^v(\mathbf{c}^t, x)})$.

Assumption 3.1. We assume that the percentile of a subject remains stationary between observations at two nearby time points, i.e., the cumulative distribution, F , should be stationary: $F(y^t) = F(y^{t+1})$.

An intuitive example for Assumption 3.1 is that if a child has the largest airway among all 2-year-olds, it is likely that this child's airway will remain the largest over a

short period of time. Therefore, an approximate individualized prediction can be obtained as $y^{t+1} \approx f^m(\mathbf{c}^{t+1}, x) + \sqrt{\frac{f^v(\mathbf{c}^{t+1}, x)}{f^v(\mathbf{c}^t, x)}}(y^t - f^m(\mathbf{c}^t, x))$.

4 EXPERIMENTS

We aim to answer the following questions with our experiments: ① *How well can *LucidAtlas* estimate population trends?* ② *Can *LucidAtlas* capture heteroscedastic variances across a population?* ③ *Do explanations from *LucidAtlas* align with our prior knowledge?* ④ *Is accepting the independence assumption unquestioningly and directly using NAMs appropriate in scientific discovery?* ⑤ *How well can *LucidAtlas* predict responses at time B given observations at an earlier time A ?*

4.1 DATASETS & EXPERIMENTAL PROTOCOLS

Learning a pediatric airway atlas is the primary motivating problem of our work [Hong et al., 2013]. We also use the OASIS brain dataset [Marcus et al. 2007] to validate our approach. The Supplementary Material provides more details about these two datasets and our experimental settings in Sec. S.4.

Pediatric Airway Geometry. The dataset includes 358 upper airway shapes obtained from computed tomography (CT) images of children with radiographically normal airways. These 358 airway shapes correspond to 264 patients, with 34 having longitudinal observations and 230 who are observed only once. We consider three covariates in this study: age, weight, and height. The majority of the missing data occur in height and the field of view of the airway. Each complete airway has 11 anatomical landmarks, of which 6 are used in our experiments (Fig. 1); 263 scans have complete covariate data (age, weight, height).

We aim to construct an airway atlas which captures airway cross sectional area (CSA) as well as CSA population distributions, incorporating the prior knowledge that CSA should monotonically increase with age, weight, and height.

We convert the k^{th} airway shape into a CSA function mapping normalized depth $x \in [0, 1]$ to CSA values as $CSA = C_k(x)$. Based on our discretization complete airways have 500 depth-CSA pairs uniformly distributed on the airway centerline, while incomplete ones have ≤ 500 .

The dataset is split into 80%/20% training / test sets respectively by patient, with all longitudinal data in the test set. This ensures that the model learns population trends from individual observations while retaining longitudinal data for individual evaluations.

OASIS Brain Volumes. Brain segmentations were obtained from the OASIS dataset [Marcus et al., 2007], which

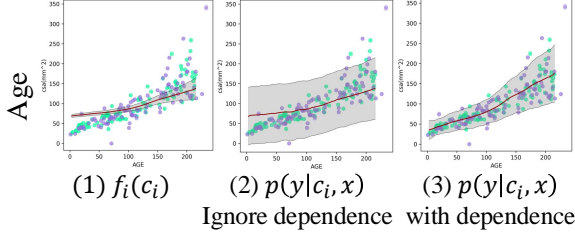


Figure 2: Visualizations of Covariate Interpretations from *LucidAtlas* for CSA Distribution at the Subglottis Landmark (Pediatric Airway Dataset). (1) $f_i(c_i)$ represents the disentangled covariate effect directly from a NAM as illustrated in Sec. 3.2.2; (2) Marginalized covariate interpretation without accounting for covariate dependence; (3) Marginalized covariate interpretation incorporating covariate dependence. Green and purple dots indicate training and testing samples respectively. The red lines represent the learned population trend, and the gray shading spans $\pm 2 \times$ standard deviations. Considering covariate dependence is essential for accurately capturing how each covariate influences the population trend and associated uncertainties.

includes two subsets: ① A cross-sectional set with 416 subjects aged 18–96, primarily single-time observations, plus a reliability subset of 20 non-demented subjects rescanned within 90 days. ② A longitudinal set of 150 older adults (60–96 years), totaling 373 imaging sessions.

Our experiments include four covariates: age, socioeconomic status (SES), mini-mental state examination (MMSE), and clinical dementia rating (CDR). The response variable is the normalized whole brain volume (nWBV).

We aim to investigate the relationships between these covariates and brain volume. Based on prior knowledge, brain volume should not increase with age or CDR, nor decrease when mental state improves [Fotenos et al., 2008].

Comparison Methods. We choose the current state-of-the-art explainable regression methods, i.e., LightGBM [Ke et al., 2017] and Explainable Boosting Machines (EBM) [Lou et al., 2013] to provide high-quality regression performance. We also compare *LucidAtlas* with NAM with Exu activations and ensembling strategies [Agarwal et al., 2020]. We found that NAMLSS performs best for learning population trends, justifying our choice of an additive structure. Besides NAMLSS for uncertainty estimation, we also directly use a multi-layer perceptron (MLP) for mean-variance parameterization of the negative log-likelihood loss as a baseline, termed MLP+NLL. I.e., this MLP+NLL model does not assume an additive structure.

Evaluation Metrics. The Mean Absolute Relative Percent Difference (MARPD) evaluates regression accuracy in capturing population trends, while the Negative Log-Likelihood (NLL) assesses how closely the modeled distribution aligns with the true data distribution.

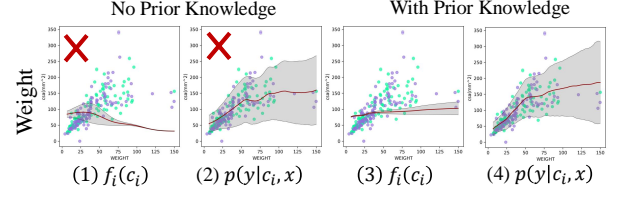


Figure 3: Visualizations of the Effect of Prior Knowledge in *LucidAtlas* at the Subglottis Landmark (Pediatric Airway Dataset). The \times symbol indicates the covariate interpretation contradicts prior knowledge, such as the NAM incorrectly interpreting airway CSA as decreasing with a child’s weight. Without incorporating prior knowledge, the model may deviate from our prior assumptions. Without marginalization, to account for covariate dependencies, the data may not be fit well.

4.2 DISCUSSIONS

Population Trend Regression. Table 2 presents the quantitative evaluation of population trend regression. Notably, in the absence of a spatial variable x , such as in the OA-SIS Brain dataset, *LucidAtlas* is equivalent to NAMLSS when no prior knowledge is incorporated. NAMLSS outperforms *MLP+NLL*, highlighting the advantage of an additive network structure with uncertainty estimation in capturing population trends. Among all methods, *LucidAtlas* achieves the best performance. For the pediatric airway dataset, training with data that include missing values, as described in Sec. 3.4.1, further enhances regression accuracy. We observe that the standard deviations of the MARPD metrics in Table 2 are large, largely due to data uncertainties. Beyond regression performance, our primary concern is how well the distribution captured by *LucidAtlas* aligns with the true population distribution, as this accounts for data uncertainties. **Population Distribution.** Table 3 quantifies the performance of different approaches in estimating population distributions. Our approach outperforms all baselines, demonstrating that incorporating prior knowledge of monotonicity, as implemented in *LucidAtlas*, enhances NAMs’ capability in modeling population distributions. **Benefit of Prior Knowledge.** Fig. 3 compares covariate interpretations with and without prior knowledge in *LucidAtlas* at the subglottis landmark. While the marginalized covariate interpretations in Fig. 3(2, 4) may appear similar, disregarding prior knowledge leads to unreasonable covariate interpretations. For instance, the model erroneously interprets airway CSA as decreasing with respect to a child’s weight at the subglottis landmark. Additional visualizations are provided in the Supplementary Material. **Role of Covariate Dependence.** Table 4 and Fig. 2 examine the significance of covariate dependence in single-feature interpretation. Fig. 2 illustrates that ignoring covariate dependence results in underconfident uncertainty estimation and suboptimal population trend prediction, highlighting the necessity of incorporating covariate dependence for reliable

Methods	Spa.	Add.	Mono.	OASIS Brain	Pediatric Airway						
					Overall	nasal spine	choana	epiglottic tip	TVC	subglottis	carina
EBM	✗	✗	✓	3.1920±2.4985	38.8774±38.9116	44.0259±40.0036	41.9254±48.9492	17.7694±22.4692	20.8076±26.3942	22.3948±28.1368	25.4489±31.4176
LightGBM	✗	✗	✗	3.0289±2.4324	36.7755±35.8704	46.1999±39.9386	28.4655±29.9739	14.1479±12.1693	19.3283±16.9426	20.6356±19.1491	19.9048±23.6890
NAM	✗	✓	✗	3.3882±2.4748	37.1746±35.1216	43.8124±40.1094	37.2806±33.4382	17.4907±13.0446	21.0430±18.8356	22.5744±21.0187	21.8049±24.0872
MLP+NLL	✗	✗	✗	3.1036±2.6835	38.3364±36.8091	33.9609±26.9933	45.0381±34.6801	18.5780±17.1130	20.5003±23.1434	19.9590±23.7551	21.0536±13.8406
NAMLSS	✗	✓	✗	3.0244±2.3980	37.3115±34.7218	30.7901±25.6496	41.1237±33.3017	21.5784±17.1608	25.3131±24.5728	24.2743±24.6332	21.1646±16.1043
Ours np	✓	✓	✗	3.0244±2.3980	36.4472±35.5650	32.9029±25.5350	40.4435±33.1123	16.1585±15.4162	19.2762±23.1651	17.8992±23.5066	17.4608±12.2250
Ours part	✓	✓	✓	3.0045±2.2426	37.1696±35.6229	37.4176±27.0885	42.1177±33.8561	16.3098±15.7531	19.7589±23.1405	19.1237±23.3031	17.9994±12.3826
Ours imp	✓	✓	✓	3.0936±2.2473	36.2685±35.6709	34.1421±26.2881	42.3398±33.8903	15.2841±14.7377	19.2930±22.9405	18.6742±23.1107	17.3280±12.0628

Table 2: Quantitative Evaluation of Normalized Brain Volume Regression (OASIS Brain Dataset) and Cross-Sectional Area Regression (Pediatric Airway Dataset) with respect to Mean Absolute Relative Percent Difference (MARPD, %). We also evaluate with respect to different landmarks. The {TVC, subglottic and carina} landmarks are significant landmarks for airway obstruction analysis [Hong et al., 2013]. **Bold red values** indicate the best scores across all methods. **Bold black values** indicate the 2nd best scores of all methods. **Spa.** indicates whether spatial dependency is considered. **Add.** indicates whether a model has an additive design. **Mono.** indicates whether prior knowledge about monotonicity is used. *Ours np* refers to LucidAtlas without incorporating prior knowledge. *Ours part* denotes our model trained only on complete data, while *Ours imp* represents using the full dataset for training, including missing values. LucidAtlas performs best overall.

	Spa.	Add.	Mono.	OASIS Brain	Pediatric Airway						
					Overall	nasal spine	choana	epiglottic tip	TVC	subglottis	carina
MLP+NLL	✗	✗	✗	2.5573	1.0273	1.7403	1.7702	-0.1508	-0.0302	0.0778	0.2415
NAMLSS	✗	✗	✗	0.6714	1.0020	1.7591	1.4011	-0.0561	0.4015	0.3951	0.917
Ours np	✓	✓	✗	0.6714	0.9365	1.7796	1.4115	-0.3948	-0.1274	-0.1633	0.0331
Ours part	✓	✓	✗	0.6487	0.8467	1.9669	1.4561	-0.3043	-0.1293	-0.1185	0.0726
Ours imp	✓	✓	✓	0.6514	0.8901	1.8087	1.4542	-0.4341	-0.0065	0.0146	0.0966

Table 3: Quantitative Evaluation of Population Distribution Estimation based on Negative Log-Likelihood (NLL). Our approach achieves the best performance overall.

Covariate	Corr.	Overall	Pediatric Airway						
			nasal spine	choana	epiglottic tip	TVC	subglottis	carina	
Age	✗	0.9907	1.9341	1.4836	0.4278	0.1805	0.1673	0.5516	
Age	✓	0.8565	2.0124	1.4789	-0.183	-0.1709	-0.1777	0.1485	
Height	✗	0.9830	2.1449	1.4496	0.4049	0.2185	0.2179	0.4715	
Height	✓	0.8330	1.9187	1.3968	-0.2574	-0.1002	-0.0819	0.0968	
Weight	✗	1.0804	2.1305	1.3957	0.6239	0.4729	0.4701	0.7822	
Weight	✓	0.8813	1.9122	1.431	-0.1077	0.0004	0.0237	0.1829	

Table 4: Quantitative Comparison of Different Ways of Marginalization. NLL is computed between the marginalized covariate interpretation and the data distribution. A ✓ in the **Corr.** column indicates that covariate dependence is considered, while ✗ signifies that it is ignored. Accounting for covariate dependence improves alignment between covariate interpretation and the data distribution.

interpretation. The quantitative results in Table 4 further confirm that, marginalized covariate interpretation with dependence better aligns with the data distribution. **Individualized Prediction.** We quantify the performance of individualized predictions (to predict for $T1$ given the observation at $T0$). As described in Sec. 3.4.2, our approach, which integrates the observations at $T0$ with population trends, yields the best predictive performance. More experiment results and visualizations are available at Sec. S.6.

5 LIMITATIONS AND FUTURE WORK

LucidAtlas models population variance with a Gaussian distribution. Expanding beyond Gaussian assumptions, more flexible probabilistic frameworks—such as non-parametric approaches or mixture models—could improve expressiveness and model fits. Identifiability issues arise

Time	OASIS Brain	Pediatric Airway						
		Overall	nasal spine	choana	epiglottic tip	TVC	subglottis	carina
$T0$	1.6042	37.2944	31.2867	50.55989	11.9559	13.2770	14.2701	19.1819
Pop.	3.1563	37.8092	39.1704	45.2991	14.7017	15.2413	15.2040	17.1568
Ind.	1.4687	35.7221	31.1910	50.1397	9.2835	10.2199	11.2128	17.2563

Table 5: Mean Absolute Relative Percent Difference (in %) for Individualized Prediction. **$T0$** in the **Time** column indicates directly using the observation from the initial time point $T0$ to predict at time $T1$. **Pop.** indicates ignoring the observation at $T0$ and directly using the mean population value $f^m(c, x)$ for individualized prediction for $T1$. **Ind.** indicates our approach illustrated in Sec. 3.4.2. Individualized prediction provides the best performance for both datasets and for most landmarks.

when covariates are dependent or the latent space is redundant, potentially affecting interpretability [Zhou and Wei, 2020, Siems et al., 2023]. Addressing these concerns is crucial for ensuring well-posed solutions. Another key extension is incorporating categorical variables into uncertainty quantification, as such variables often exist for real-world datasets. Currently, we describe the airway using cross-sectional area. In future work, we plan to develop a probabilistic representation for 3D shape modeling with uncertainties by extending NAISR [Jiao et al., 2023].

6 CONCLUSIONS

We introduced LucidAtlas, an approach for learning an uncertainty-aware, covariate-disentangled, and individualized atlas representation. Additionally, we highlighted potential risks in using NAMs for covariate interpretation in the presence of covariate dependence and proposed a computationally efficient marginalization approach to mitigate these limitations. Furthermore, we found that incorporating prior knowledge helps eliminate misleading interpretations. We evaluated our method using two distinct datasets, validating its trustworthiness and effectiveness. LucidAtlas stands out as the only atlas representation capable of addressing covariate-, subject-, population-, and spatial-level questions in an interpretable and reliable manner.

7 ACKNOWLEDGEMENT

The research reported in this publication was supported by NIH grant 1R01HL154429 and 1R21HL172230-01A1. The content is solely the responsibility of the authors and does not necessarily represent the official views of the NIH.

References

- Rishabh Agarwal, Nicholas Frosst, Xuezhou Zhang, Rich Caruana, and Geoffrey E Hinton. Neural additive models: Interpretable machine learning with neural nets. *arXiv preprint arXiv:2004.13912*, 2020.
- Sercan Ö Arik and Tomas Pfister. Tabnet: Attentive interpretable tabular learning. In *Proceedings of the AAAI Conference on Artificial Intelligence*, volume 35, pages 6679–6687, 2021.
- Cosmin I Bercea, Benedikt Wiestler, Daniel Rueckert, and Shadi Albarqouni. Federated disentangled representation learning for unsupervised brain anomaly detection. *Nature Machine Intelligence*, 4(8):685–695, 2022.
- Jeroen Berrevoets, Ahmed Alaa, Zhaozhi Qian, James Jordan, Alexander ES Gimson, and Mihaela Van Der Schaar. Learning queueing policies for organ transplantation allocation using interpretable counterfactual survival analysis. In *International Conference on Machine Learning*, pages 792–802. PMLR, 2021.
- Kouroche Bouchiat, Alexander Immer, Hugo Yèche, Gunnar Rätsch, and Vincent Fortuin. Improving neural additive models with bayesian principles. *arXiv preprint arXiv:2305.16905*, 2023.
- Agisilaos Chartsias, Thomas Joyce, Giorgos Papanastasiou, Scott Semple, Michelle Williams, David E Newby, Rohan Dharmakumar, and Sotirios A Tsaftaris. Disentangled representation learning in cardiac image analysis. *Medical image analysis*, 58:101535, 2019.
- Kan Chen, Qishuo Yin, and Qi Long. Covariate-balancing-aware interpretable deep learning models for treatment effect estimation. *arXiv preprint arXiv:2203.03185*, 2022.
- Jiebin Chu, Yaoyun Zhang, Fei Huang, Luo Si, Songfang Huang, and Zhengxing Huang. Disentangled representation for sequential treatment effect estimation. *Computer Methods and Programs in Biomedicine*, 226:107175, 2022.
- Olivier Commowick, Radu Stefanescu, Pierre Fillard, Vincent Arsigny, Nicholas Ayache, Xavier Pennec, and Grégoire Malandain. Incorporating statistical measures of anatomical variability in atlas-to-subject registration for conformal brain radiotherapy. In *International Conference on Medical Image Computing and Computer-Assisted Intervention*, pages 927–934. Springer, 2005.
- Jonathan Crabbe, Zhaozhi Qian, Fergus Imrie, and Mihaela van der Schaar. Explaining latent representations with a corpus of examples. In M. Ranzato, A. Beygelzimer, Y. Dauphin, P.S. Liang, and J. Wortman Vaughan, editors, *Advances in Neural Information Processing Systems*, volume 34, pages 12154–12166. Curran Associates, Inc., 2021. URL <https://proceedings.neurips.cc/paper/2021/file/65658fde58ab3c2b6e5132a39fae7cb9-Paper.pdf>.
- Erik Daxberger, Agustinus Kristiadi, Alexander Immer, Runa Eschenhagen, Matthias Bauer, and Philipp Hennig. Laplace redux-effortless bayesian deep learning. *Advances in Neural Information Processing Systems*, 34: 20089–20103, 2021.
- Nicola De Cao, Wilker Aziz, and Ivan Titov. Block neural autoregressive flow. In *Uncertainty in artificial intelligence*, pages 1263–1273. PMLR, 2020.
- Zheng Ding, Yifan Xu, Weijian Xu, Gaurav Parmar, Yang Yang, Max Welling, and Zhuowen Tu. Guided variational autoencoder for disentanglement learning. In *Proceedings of the IEEE/CVF conference on computer vision and pattern recognition*, pages 7920–7929, 2020.
- Anthony F Fotenos, Mark A Mintun, Abraham Z Snyder, John C Morris, and Randy L Buckner. Brain volume decline in aging: evidence for a relation between socioeconomic status, preclinical Alzheimer disease, and reserve. *Archives of neurology*, 65(1):113–120, 2008.
- Jerome H Friedman. Greedy function approximation: a gradient boosting machine. *Annals of statistics*, pages 1189–1232, 2001.
- Yarin Gal and Zoubin Ghahramani. Dropout as a bayesian approximation: Representing model uncertainty in deep learning. In *international conference on machine learning*, pages 1050–1059. PMLR, 2016.
- Trevor J Hastie. *Generalized additive models*. Routledge, 2017.
- Yi Hong, Marc Niethammer, Johan Andrieu, Julia S Kimbell, Elizabeth Pitkin, Richard Superfine, Stephanie Davis, Carlton J Zdanski, and Brad Davis. A pediatric airway atlas and its application in subglottic stenosis. In *2013 Ieee 10th International Symposium on Biomedical Imaging*, pages 1206–1209. IEEE, 2013.
- Eyke Hüllermeier and Willem Waegeman. Aleatoric and epistemic uncertainty in machine learning: An introduction to concepts and methods. *Machine learning*, 110(3): 457–506, 2021.
- Alexander Immer, Emanuele Palumbo, Alexander Marx, and Julia Vogt. Effective bayesian heteroscedastic regression with deep neural networks. *Advances in Neural Information Processing Systems*, 36, 2024.
- Clifford R Jack Jr, Matt A Bernstein, Nick C Fox, Paul Thompson, Gene Alexander, Danielle Harvey, Bret

- Borowski, Paula J Britson, Jennifer L. Whitwell, Chadwick Ward, et al. The Alzheimer’s disease neuroimaging initiative (ADNI): MRI methods. *Journal of Magnetic Resonance Imaging: An Official Journal of the International Society for Magnetic Resonance in Medicine*, 27(4):685–691, 2008.
- Yining Jiao, Carlton Zdanski, Julia Kimbell, Andrew Prince, Cameron Worden, Samuel Kirse, Christopher Rutter, Benjamin Shields, William Dunn, Jisan Mahmud, et al. Naisr: A 3D neural additive model for interpretable shape representation. *arXiv preprint arXiv:2303.09234*, 2023.
- Ze Jin, Jayaram K Udupa, and Drew A Torigian. How many models/atlas are needed as priors for capturing anatomic population variations? *Medical image analysis*, 58:101550, 2019.
- Vineet John, Lili Mou, Hareesh Bahuleyan, and Olga Vechtomova. Disentangled representation learning for non-parallel text style transfer. *arXiv preprint arXiv:1808.04339*, 2018.
- Sarang Joshi, Brad Davis, Matthieu Jomier, and Guido Gerig. Unbiased diffeomorphic atlas construction for computational anatomy. *NeuroImage*, 23:S151–S160, 2004.
- Hyungsik Jung and Youngrock Oh. Towards better explanations of class activation mapping. In *Proceedings of the IEEE/CVF International Conference on Computer Vision*, pages 1336–1344, 2021.
- Guolin Ke, Qi Meng, Thomas Finley, Taifeng Wang, Wei Chen, Weidong Ma, Qiwei Ye, and Tie-Yan Liu. Lightgbm: A highly efficient gradient boosting decision tree. *Advances in neural information processing systems*, 30, 2017.
- Ouail Kitouni, Niklas Nolte, and Michael Williams. Expressive monotonic neural networks. *arXiv preprint arXiv:2307.07512*, 2023.
- N Kovačević, JT Henderson, E Chan, N Lifshitz, J Bishop, AC Evans, RM Henkelman, and XJ Chen. A three-dimensional MRI atlas of the mouse brain with estimates of the average and variability. *Cerebral cortex*, 15(5): 639–645, 2005.
- Balaji Lakshminarayanan, Alexander Pritzel, and Charles Blundell. Simple and scalable predictive uncertainty estimation using deep ensembles. *Advances in neural information processing systems*, 30, 2017.
- Xingchao Liu, Xing Han, Na Zhang, and Qiang Liu. Certified monotonic neural networks. *Advances in Neural Information Processing Systems*, 33:15427–15438, 2020.
- Yin Lou, Rich Caruana, Johannes Gehrke, and Giles Hooker. Accurate intelligible models with pairwise interactions. In *Proceedings of the 19th ACM SIGKDD international conference on Knowledge discovery and data mining*, pages 623–631, 2013.
- Xiaoyu Lu, Alexis Boukouvalas, and James Hensman. Additive gaussian processes revisited. In *International Conference on Machine Learning*, pages 14358–14383. PMLR, 2022.
- Scott Lundberg. A unified approach to interpreting model predictions. *arXiv preprint arXiv:1705.07874*, 2017.
- Daniel S Marcus, Tracy H Wang, Jamie Parker, John G Csernansky, John C Morris, and Randy L Buckner. Open access series of imaging studies (oasis): cross-sectional MRI data in young, middle aged, nondemented, and demented older adults. *Journal of cognitive neuroscience*, 19(9):1498–1507, 2007.
- Raha Moraffah, Mansooreh Karami, Ruocheng Guo, Adrienne Raglin, and Huan Liu. Causal interpretability for machine learning-problems, methods and evaluation. *ACM SIGKDD Explorations Newsletter*, 22(1):18–33, 2020.
- Harsha Nori, Samuel Jenkins, Paul Koch, and Rich Caruana. Interpretml: A unified framework for machine learning interpretability, 2019. URL <https://arxiv.org/abs/1909.09223>.
- Marco Tulio Ribeiro, Sameer Singh, and Carlos Guestrin. "Why should i trust you?" Explaining the predictions of any classifier. In *Proceedings of the 22nd ACM SIGKDD international conference on knowledge discovery and data mining*, pages 1135–1144, 2016.
- Olaf Ronneberger, Philipp Fischer, and Thomas Brox. U-net: Convolutional networks for biomedical image segmentation. In *Medical image computing and computer-assisted intervention–MICCAI 2015: 18th international conference, Munich, Germany, October 5-9, 2015, proceedings, part III 18*, pages 234–241. Springer, 2015.
- Cynthia Rudin. Stop explaining black box machine learning models for high stakes decisions and use interpretable models instead. *Nature machine intelligence*, 1(5):206–215, 2019.
- Davor Runje and Sharath M Shankaranarayana. Constrained monotonic neural networks. In *International Conference on Machine Learning*, pages 29338–29353. PMLR, 2023.
- Alon Shoshan, Nadav Bhonker, Igor Kviatkovsky, and Gerard Medioni. GAN-control: Explicitly controllable GANs. In *Proceedings of the IEEE/CVF international conference on computer vision*, pages 14083–14093, 2021.

- Julien Siems, Konstantin Ditschuneit, Winfried Ripken, Alma Lindborg, Maximilian Schambach, Johannes Otterbach, and Martin Genzel. Curve your enthusiasm: concavity regularization in differentiable generalized additive models. *Advances in Neural Information Processing Systems*, 36:19029–19057, 2023.
- Andrew Stirn, Hans-Hermann Wessels, Megan Schertzer, Laura Pereira, Neville E. Sanjana, and David A. Knowles. Faithful heteroscedastic regression with neural networks, 2022. URL <https://arxiv.org/abs/2212.09184>.
- Jayaraman J Thiagarajan, Prasanna Sattigeri, Deepta Rajan, and Bindya Venkatesh. Calibrating healthcare AI: Towards reliable and interpretable deep predictive models. *arXiv preprint arXiv:2004.14480*, 2020.
- Anton Frederik Thielmann, René-Marcel Kruse, Thomas Kneib, and Benjamin Säfken. Neural additive models for location scale and shape: A framework for interpretable neural regression beyond the mean. In *International Conference on Artificial Intelligence and Statistics*, pages 1783–1791. PMLR, 2024.
- Paul M Thompson and Arthur W Toga. A framework for computational anatomy. *Computing and Visualization in Science*, 5(1):13–34, 2002.
- Tianyang Wang, Yunze Wang, Jun Zhou, Benji Peng, Xinyuan Song, Charles Zhang, Xintian Sun, Qian Niu, Junyu Liu, Silin Chen, et al. From aleatoric to epistemic: Exploring uncertainty quantification techniques in artificial intelligence. *arXiv preprint arXiv:2501.03282*, 2025.
- Sanghyun Woo, Jongchan Park, Joon-Young Lee, and In So Kweon. Cbam: Convolutional block attention module. In *Proceedings of the European conference on computer vision (ECCV)*, pages 3–19, 2018.
- Jeffrey M Wooldridge, Mokhtarul Wadud, and Jenny Lye. *Introductory econometrics: Asia pacific edition with on-line study tools 12 months*. Cengage AU, 2016.
- Mutian Xu, Junhao Zhang, Zhipeng Zhou, Mingye Xu, Xiaojuan Qi, and Yu Qiao. Learning geometry-disentangled representation for complementary understanding of 3d object point cloud. In *Proceedings of the AAAI Conference on Artificial Intelligence*, volume 35, pages 3056–3064, 2021.
- Jie Yang, Kaichun Mo, Yu-Kun Lai, Leonidas J Guibas, and Lin Gao. Dsm-net: Disentangled structured mesh net for controllable generation of fine geometry. *arXiv preprint arXiv:2008.05440*, 2(3), 2020.
- Seungil You, David Ding, Kevin Canini, Jan Pfeifer, and Maya Gupta. Deep lattice networks and partial monotonic functions. *Advances in neural information processing systems*, 30, 2017.
- Xiuming Zhang, Zhoutong Zhang, Chengkai Zhang, Josh Tenenbaum, Bill Freeman, and Jiajun Wu. Learning to reconstruct shapes from unseen classes. *Advances in neural information processing systems*, 31, 2018a.
- Yuting Zhang, Yijie Guo, Yixin Jin, Yijun Luo, Zhiyuan He, and Honglak Lee. Unsupervised discovery of object landmarks as structural representations. In *Proceedings of the IEEE Conference on Computer Vision and Pattern Recognition*, pages 2694–2703, 2018b.
- Bolei Zhou, Aditya Khosla, Agata Lapedriza, Aude Oliva, and Antonio Torralba. Learning deep features for discriminative localization. In *Computer Vision and Pattern Recognition*, 2016.
- Ding Zhou and Xue-Xin Wei. Learning identifiable and interpretable latent models of high-dimensional neural activity using pi-vae. *Advances in Neural Information Processing Systems*, 33:7234–7247, 2020.
- Özgün Çiçek, Ahmed Abdulkadir, Soeren S. Lienkamp, Thomas Brox, and Olaf Ronneberger. 3D u-net: Learning dense volumetric segmentation from sparse annotation, 2016. URL <https://arxiv.org/abs/1606.06650>.

SUPPLEMENTARY MATERIAL FOR LUCIDATLAS

S.1 EXTENDED RELATED WORK

Epistemic Uncertainty versus Aleatoric Uncertainty. Epistemic and aleatoric uncertainties are two different kinds of uncertainties. Epistemic uncertainty relates to model parameters and stems from limited model knowledge, which is reducible with more data or better modeling. Important techniques include the Laplace approximation [Daxberger et al., 2021], Ensembling [Hüllermeier and Waegeman, 2021] and MC-Dropout [Gal and Ghahramani, 2016]. Aleatoric uncertainty arises from inherent data randomness and is irreducible. Important techniques includes a line of Bayesian Neural Networks [Stirn et al., 2022, Immer et al., 2024]. DeepEnsembles [Lakshminarayanan et al., 2017] can handle both epistemic and aleatoric uncertainties.

Regarding uncertainty estimation for interpretable models, more attention is paid to epistemic uncertainties. NAMs used ensembling to estimate and decrease model uncertainties [Agarwal et al., 2020]. LA-NAM used Laplace approximations for uncertainty estimation [Bouchiat et al., 2023] with NAMs. In atlas construction, aleatoric uncertainty is especially important when individual differences are large. Capturing aleatoric uncertainty is crucial in medicine to understand population variations. NAMLSS can model aleatoric uncertainty using NAMs to approximate the parameters $\{\theta^k\}$ of a data distribution [Thielmann et al., 2024], as

$$\theta^{(k)} = h^{(k)} \left(\beta^{(k)} + \sum_{i=1}^N f_i^{(k)}(c_i) \right) \quad (\text{S.15})$$

where $\theta^{(k)}$ can, for example, be the mean and variance of Gaussian distributions; $\beta^{(k)}$ denotes the parameter-specific intercept and $f_i^{(k)}$ represents the feature network for parameter k for the i -th feature. *LucidAtlas extends NAMLSS to a more versatile representation, enabling individualized prediction, incorporating prior knowledge, and capturing spatial dependence.*

Monotonicity. Monotonic neural networks ensure that a network’s output changes monotonically with respect to certain inputs. Research has focused on two lines of approaches: architectures such as Deep Lattice Networks [You et al., 2017] that guarantee monotonicity but may lack expressiveness, and heuristic methods such as Certified Monotonic Neural Networks [Liu et al., 2020] that use regularization but can be computationally expensive. Recent advancements, including Constrained Monotonic Neural Networks [Runje and Shankaranarayana, 2023], aim to balance monotonicity, expressiveness, and efficiency. Additionally, research in normalizing flows [De Cao et al., 2020] has contributed to developing monotonic functions in neural networks to ensure invertibility. Expressive monotonic neural networks [Kitouni et al., 2023] are constructed using Lipschitz-constrained neural networks, ensuring monotonicity by design while preserving expressiveness. *We use the Lpshitz-constrained neural networks to ensure monotonicity in LucidAtlas to follow prior / domain knowledge.*

Disentangled Representation Learning. Disentangled representation learning (DRL) has been explored in a variety of domains, including computer vision [Shoshan et al., 2021, Ding et al., 2020, Zhang et al., 2018b,a, Xu et al., 2021, Yang et al., 2020], natural language processing [John et al., 2018], and medical image analysis [Chartsias et al., 2019, Bercea et al., 2022].

Medical data is typically associated with various covariates which should be taken into account during analyses. Taking [Chu et al., 2022] as an example, when observing a tumor’s progression, it is difficult to know whether the variation of a tumor’s progression is due to time-varying covariates or due to treatment effects. Therefore, being able to disentangle different effects is highly useful for a representation to promote understanding and to be able to quantify the effect of covariates on observations. *LucidAtlas disentangles covariate effects in terms of their contribution to population trends and uncertainties.*

Explainable Artificial Intelligence. The goal of eXplainable Artificial Intelligence (XAI) is to provide human-understandable explanations for the decisions and actions of AI models. Various approaches to XAI have been proposed, including counterfactual inference [Berrevoets et al., 2021, Moraffah et al., 2020, Thiagarajan et al., 2020, Chen et al., 2022], attention maps [Zhou et al., 2016, Jung and Oh, 2021, Woo et al., 2018], feature importance [Arik and Pfister, 2021, Ribeiro et al., 2016, Agarwal et al., 2020], and instance retrieval [Crabbe et al., 2021]. A neural additive model (NAM) [Agarwal et al., 2020, Jiao et al., 2023] is an important XAI method that achieves interpretability through a linear combination of neural networks, each focusing on a *single* input feature. NAISR pioneers the use of NAMs for modeling medical shapes to enable scientific discoveries in the medical domain [Jiao et al., 2023]; however, it does not account for heteroskedasticity in

Notations	Explanations
y	Observed variable, i.e., target variable to model
\mathbf{c}	A vector containing all N covariates, e.g, $\mathbf{c} = [age, weight, \dots]$
$f^m(\mathbf{c}, x)$ or f^m	Prediction of mean population trend given \mathbf{c} at location x
$f_i^m(c_i, x)$ or f_i^m	Additive effects predicted from i^{th} subnetwork f_i for mean
$f^v(\mathbf{c}, x)$ or f^v	Prediction of population variance given \mathbf{c} at location x
$f_i^v(c_i, x)$ or f_i^v	Additive effects predicted from i^{th} subnetwork f_i for variance
$g_{i,k}^m(c_i)$	The predicted mean of c_k given c_i
$g_{i,k}^v(c_i)$	The predicted variance of c_k given c_i
$p(y c_i, x)$	Marginalized covariate effects: how c_i affect y at location x
$E[y c_i, x]$	The expectation of y when c_i and x are fixed
$Var(y c_i, x)$	The variance of y when c_i and x are fixed

Table S.6: Illustrations of the Notations.

its shape representation and does not consider uncertainties. *LucidAtlas* extends this concept by integrating NAMs to construct an atlas that captures population trends and uncertainties with spatial dependencies.

S.2 METHOD

S.2.1 NOTATIONS

Table S.6 shows the notations used in this paper.

S.2.2 EXPANDED DISCUSSION ON THE TOY EXAMPLE

Assuming c_1 and c_2 are covariates that influence the observed result y , a NAM fits well whose subnetworks capture $f_1(c_1) = \sin(c_1)$ and $f_2(c_2) = c_2$ and thus approximate y with $y \approx f(c_1, c_2) + \epsilon = f_1(c_1) + f_2(c_2) + \epsilon$, where ϵ is Gaussian noise with mean zero.

If we want to interpret the population trend of y with only c_1 , we need to marginalize c_2 out as

$$\begin{aligned}
F_1(c_1) &= \int_{-\infty}^{\infty} [f_1(c_1) + f(c_2)]p(c_2|c_1) dc_2 \\
&= \underbrace{f_1(c_1)}_{\text{Interpretation from NAMs}} + \underbrace{\int_{-\infty}^{\infty} f_2(c_2)p(c_2|c_1) dc_2}_{\text{Interpretation from Dependence: } := h_1(c_1)} \\
&= \sin(c_1) + \int_{-\infty}^{\infty} c_2 p(c_2|c_1) dc_2
\end{aligned} \tag{S.16}$$

where $h_1(c_1)$ measures how the dependence between c_1 and c_2 influences the marginalization $F_1(c_1)$. We can see from Eq. S.16 that $F_1(c_1)$ is composed of the interpretation from the NAM's subnetwork plus the interpretation from the dependence between c_1 and c_2 as $h_1(c_1)$.

If we want to interpret the population trend of y with only c_2 , we need to marginalize c_1 out as

$$\begin{aligned}
F_2(c_2) &= \int_{-\infty}^{\infty} [f_2(c_2) + f(c_1)]p(c_1|c_2) dc_1 \\
&= \underbrace{f_2(c_2)}_{\text{Interpretation from NAMs}} + \underbrace{\int_{-\infty}^{\infty} f_1(c_1)p(c_1|c_2) dc_1}_{\text{Interpretation from Dependence: } := h_2(c_2)} \\
&= c_2 + \int_{-\infty}^{\infty} \sin(c_1)p(c_1|c_2) dc_1 .
\end{aligned} \tag{S.17}$$

If c_1 and c_2 are independent,

$$h_1(c_1) = \int_{-\infty}^{\infty} f_2(c_2)p(c_2|c_1) dc_2 = \int_{-\infty}^{\infty} f_2(c_2)p(c_2) dc_2 = E_{p(c_2)}[f_2(c_2)] = f_2(E[c_2]) = E[c_2] = \text{constant} , \tag{S.18}$$

$$h_2(c_2) = \int_{-\infty}^{\infty} f_1(c_1)p(c_1|c_2) dc_1 = \int_{-\infty}^{\infty} f_1(c_1)p(c_1) dc_1 = E_{p(c_1)}[f_1(c_1)] = f_1(E[c_1]) = \sin(E[c_1]) = \text{constant} . \tag{S.19}$$

Thus

$$\begin{aligned}
F_1(c_1) &= \sin(c_1) + E[c_2] \\
F_2(c_2) &= c_2 + \sin(E[c_1])
\end{aligned} \tag{S.20}$$

which means the marginalization is the actual covariate disentanglement in Sec. 3.2.2 plus a constant.

If c_1 and c_2 are dependent

$h(c_1)$ is a function of c_1 which is controlled by the dependence between c_1 and c_2 .

For example, assume the relationship between c_1 and c_2 are at one extreme of dependence in the sense that c_2 is a deterministic function of c_1 as

$$c_2 = \exp(c_1) . \tag{S.21}$$

Then

$$\begin{aligned}
F_1(c_1) &= \sin(c_1) + \int_{-\infty}^{\infty} c_2 p(c_2|c_1) dc_2 \\
&= \sin(c_1) + \exp(c_1)
\end{aligned} \tag{S.22}$$

$$\begin{aligned}
F_2(c_2) &= c_2 + \int_{-\infty}^{\infty} \sin(c_1)p(c_1|c_2) dc_1 \\
&= c_2 + \sin(\log(x_2)) .
\end{aligned} \tag{S.23}$$

Therefore, considering the relationship between c_1 and c_2 is crucial when using either covariate to interpret the population trend.

In summary, disentangled covariate effects of NAMs, combined with those effects contributed by covariate dependence, shape human-understandable explanations aligned with population trends. *While ignoring potential dependencies in NAMs may not impact prediction performance, it can result in ambiguous or misleading interpretations when analyzing population trends.*

S.2.3 COVARIATE MARGINALIZATION

This section introduces our proposed marginalization approach to improve the trustworthiness of NAMs when trying to understand the dependency of a covariate on the response. The dependency of covariates can be modeled with a multivariate Gaussian distribution as $p(\mathbf{c}|c_i) = \mathcal{N}(\hat{\boldsymbol{\mu}}(c_i), \hat{\boldsymbol{\Sigma}}(c_i))$ where $\hat{\boldsymbol{\mu}}(c_i)$ represents the mean vector and $\hat{\boldsymbol{\Sigma}}(c_i)$ the covariance matrix conditioned on c_i . From $p(\mathbf{c}|c_i)$, one can extract the distribution of an individual covariate c_k conditioned on c_i , as $p(c_k|c_i) = \mathcal{N}(\hat{\mu}_k(c_i), \hat{\Sigma}_{k,k}(c_i))$, e.g., how age c_i determines weight c_k . One can also extract the joint distribution of c_{K_1} and c_{K_2} conditioned on c_i as $p(c_{K_1}, c_{K_2}|c_i)$ from $p(\mathbf{c}|c_i)$, i.e.,

$$p(c_{K_1}, c_{K_2}|c_i) = \mathcal{N}\left(\begin{bmatrix} \hat{\mu}_{K_1}(c_i) \\ \hat{\mu}_{K_2}(c_i) \end{bmatrix}, \begin{bmatrix} \hat{\Sigma}_{K_1, K_1}(c_i) & \hat{\Sigma}_{K_1, K_2}(c_i) \\ \hat{\Sigma}_{K_2, K_1}(c_i) & \hat{\Sigma}_{K_2, K_2}(c_i) \end{bmatrix}\right), \quad (\text{S.24})$$

where $\hat{\Sigma}_{K_1, K_2}(c_i)$ is the covariance between c_{K_1} and c_{K_2} .

If the covariates are independent with each other, $\hat{\boldsymbol{\Sigma}}$ is a diagonal matrix.

We employ subnetworks $\{g_i(c_i)\}$, each controlled by an individual covariate c_i , to model the corresponding conditional distributions $\{p(\mathbf{c}|c_i)\}$. Specifically, each subnetwork $g_i(c_i)$ captures a multivariate Gaussian distribution, expressed as: $p(\mathbf{c}|c_i) = \mathcal{N}(g_i^m(c_i), g_i^v(c_i))$, where the mean vector $g_i^m(c_i)$ and the covariance matrix $g_i^v(c_i)$ are predicted by $g_i(c_i)$, as illustrated in Fig. 1.

Next, from Eq. (S.15), the observation y can be formulated as

$$y = f^m(\mathbf{c}, x) + f^v(\mathbf{c}, x) \cdot \epsilon, \quad \epsilon \sim \mathcal{N}(0, 1). \quad (\text{S.25})$$

With trained $\{f_i\}$ and $\{g_i\}$, we now investigate how c_i influences the distribution of the observation y as $p(y|c_i, x) = \mathcal{N}(\tilde{\mu}(c_i, x), \tilde{\sigma}^2(c_i, x))$, where $\tilde{\mu}(c_i, x)$ is the expectation of y when fixing c_i and x , i.e. $\mathbb{E}[y|c_i, x]$; and $\tilde{\sigma}^2(c_i, x)$ is the variance of y when fixing c_i and x , i.e. $\text{Var}(y|c_i, x)$.

Mean of $p(y|c_i, x)$. We expand the two variable case in Sec. 3.3 to multi-covariates, with the *law of total expectation* (1)

$$\begin{aligned} \tilde{\mu}(c_i, x) &= \mathbb{E}[y|c_i, x] = \mathbb{E}[(f^m(\mathbf{c}, x) + f^v(\mathbf{c}, x) \cdot \epsilon)|c_i, x] \\ &\stackrel{(1)}{=} \mathbb{E}[f^m(\mathbf{c}, x)|c_i, x] = \int_{-\infty}^{\infty} f^m(\mathbf{c}, x) p(\mathbf{c}_{k \neq i}|c_i) d\mathbf{c}_{k \neq i} \\ &= \int_{-\infty}^{\infty} \left(\sum_{k=1}^N f_k^m(c_k, x) \right) p(\mathbf{c}_{k \neq i}|c_i) d\mathbf{c}_{k \neq i} \\ &= f_i^m(c_i, x) + \underbrace{\int_{-\infty}^{\infty} \left(\sum_{k \neq i} f_k^m(c_k, x) \right) p(\mathbf{c}_{k \neq i}|c_i) d\mathbf{c}_{k \neq i}}_{:=H} \end{aligned} \quad (\text{S.26})$$

where $f_k^m(c_k)$ represents the interpretation from the additive subnetwork f_i of LucidAtlas, while H accounts for the contributions from the dependencies between the covariates which can be further simplified as follows

$$\begin{aligned} H &= \sum_{k \neq i} \int_{-\infty}^{\infty} f_k^m(c_k, x) p(\mathbf{c}_{k \neq i}|c_i) d\mathbf{c}_{k \neq i} \\ &= \sum_{k \neq i} \int_{-\infty}^{\infty} f_k^m(c_k, x) \left(\int_{-\infty}^{\infty} p(\mathbf{c}_{j \neq \{i, k\}}, c_k|c_i) d\mathbf{c}_{j \neq \{i, k\}} \right) dc_k \\ &= \sum_{k \neq i} \int_{-\infty}^{\infty} f_k^m(c_k, x) p(c_k|c_i) dc_k \end{aligned} \quad (\text{S.27})$$

where $\mathbf{c}_{k \neq i} = [c_1, \dots, c_{i-1}, c_{i+1}, \dots, c_N]$.

Eq. (S.27) indicates that even when multiple covariates are involved, only conditional dependencies with respect to individual covariates ($p(c_k|c_i)$) are required to compute $\tilde{\mu}(c_i, x)$ as a consequence of the additive model for a NAM, which simplifies computations.

Therefore,

$$\tilde{\mu}(c_i, x) = f_i^m(c_i, x) + \sum_{k \neq i} \int_{-\infty}^{\infty} f_k^m(c_k, x) p(c_k|c_i) dc_k. \quad (\text{S.28})$$

Variance of $p(y|c_i, x)$. The law of total variance is $\text{Var}(Y) = \text{E}[\text{Var}(Y|X)] + \text{Var}(\text{E}[Y|X])$ which states that the total variance of a random variable Y can be broken into two parts: ① the **expected variance of Y given X** , which represents how much Y fluctuates around its mean for each specific value of X ; and ② The variance of the **expected value of Y given X** , which measures how much the mean of Y changes as X varies. With the law of total variance,

$$\text{Var}(y|c_i, x) = \underbrace{\text{E}[\text{Var}(y|\mathbf{c}_{k \neq i}, c_i, x)]}_{\textcircled{1} := \tilde{\sigma}_E^2(c_i, x)} + \underbrace{\text{Var}(\text{E}[y|\mathbf{c}_{k \neq i}, c_i, x])}_{\textcircled{2} := \tilde{\sigma}_V^2(c_i, x)} \quad (\text{S.29})$$

The expected variance of $f^v(\mathbf{c}, x)$ given c_i and x is

$$\begin{aligned} \tilde{\sigma}_E^2(c_i, x) &= \text{E}[\text{Var}(y|\mathbf{c}_{k \neq i}, c_i, x)] = \text{E}[f^v(\mathbf{c}, x)|c_i, x] \\ &= \int_{-\infty}^{\infty} f^v(\mathbf{c}, x) p(\mathbf{c}_{k \neq i}|c_i) d\mathbf{c}_{k \neq i} \\ &= f_i^v(c_i, x) + \sum_{k \neq i} \int_{-\infty}^{\infty} f_k^v(c_k, x) p(c_k|c_i) dc_k. \end{aligned} \quad (\text{S.30})$$

And the variance of the expected value of $f^m(\mathbf{c}, x)$ given c_i and x can be computed as

$$\begin{aligned} \tilde{\sigma}_V^2(c_i, x) &= \text{Var}(\text{E}[y|\mathbf{c}_{k \neq i}, c_i, x]) = \text{Var}(f^m(c_i, \mathbf{c}_{k \neq i}, x)|c_i) \\ &= \text{Var}(f_i^m(c_i, x) + \sum_{k \neq i} f_k^m(c_k, x)|c_i, x) \\ &= \text{Var}(\sum_{k \neq i} f_k^m(c_k, x)|c_i, x) \\ &= \sum_{k \neq i} \underbrace{\text{Var}(f_k^m(c_k, x)|c_i, x)}_{\textcircled{3}} \\ &\quad + \sum_{K_1 \neq K_2 \neq i} \underbrace{\text{Cov}(f_{K_1}^m(c_{K_1}, x), f_{K_2}^m(c_{K_2}, x)|c_i, x)}_{\textcircled{4}} \end{aligned} \quad (\text{S.31})$$

where

$$\begin{aligned} \textcircled{3} &= \int_{-\infty}^{\infty} (f_k^m(c_k, x) - \tilde{\mu}_k(c_i, x))^2 p(c_k|c_i) dc_k, \\ \tilde{\mu}_k(c_i, x) &= \int_{-\infty}^{\infty} f_k^m(c_k, x) p(c_k|c_i) dc_k \end{aligned} \quad (\text{S.32})$$

$$\begin{aligned} \textcircled{4} &= \int_{-\infty}^{\infty} \int_{-\infty}^{\infty} f_{K_1}^m(c_{K_1}, x) f_{K_2}^m(c_{K_2}, x) p(c_{K_1}, c_{K_2}|c_i) dc_{K_1} dc_{K_2} \\ &\quad - \tilde{\mu}_{K_1}(c_i, x) \tilde{\mu}_{K_2}(c_i, x) \end{aligned} \quad (\text{S.33})$$

Eqs. (S.30)-(S.33) imply that instead of sampling the entire covariate space, one only needs to sample from the joint Gaussian distribution between the two covariates, conditioned on the individual covariates, to obtain the marginalized distribution $p(y|c_i, x)$.

Approximation. The integrals in $\tilde{\mu}(c_i, x)$ (in Eq. (S.28)), $\tilde{\sigma}_E^2(c_i, x)$ (in Eq. (S.30)) and $\tilde{\sigma}_V^2(c_i, x)$ (in Eqs. (S.30)-(S.33)) can be approximated using Monte Carlo sampling. E.g. for $\tilde{\mu}(c_i, x)$, for each covariate c_k one can sample L values $\{\hat{c}_k^l\}_{l=1, \dots, L}$ from the distribution of covariates $p(c_k|c_i)$ given by $g_k(\cdot)$ to approximate $\tilde{\mu}(c_i, x)$ as

$$\tilde{\mu}(c_i, x) \approx f_i^m(c_i) + \frac{1}{L} \sum_{k \neq i} \sum_{l=1}^L f_k^m(\hat{c}_k^l, x), \quad (\text{S.34})$$

where the $\{\hat{c}_k^l\}_{l=1}^L$ are sampled from $p(c_k|c_i)$.

Computational Complexity. Suppose there are N covariates and L samples. The computational complexity of marginalizing the NAM for a covariate is $\mathcal{O}(LN)$, making it feasible in practice. In contrast, for a black-box model, which does not assume our additive structure, the complexity is exponentially higher at $\mathcal{O}(L^N)$, making direct computation infeasible for large N .

As a result, we obtain $\tilde{\mu}(c_i, x)$ and $\tilde{\sigma}^2(c_i, x) = \tilde{\sigma}_E^2(c_i, x) + \tilde{\sigma}_V^2(c_i, x)$ to parameterize $p(y|c_i) = \mathcal{N}(\tilde{\mu}(c_i, x), \tilde{\sigma}^2(c_i, x))$, capturing the influence of a single covariate c_i on the observation y . Our approach aligns with NAM interpretations and can be applied post-hoc.

S.2.3.1 Imputation

Our approach naturally facilitates the imputation of missing covariates, as it inherently predicts the conditional distributions $\{p(c_k | c_i)\}$, enabling a principled way to estimate missing values. Specifically, if c_i is missing, one can choose the g_s whose uncertainty is the smallest as the predictor for c_i as $s \leftarrow \arg \min_{k, k \neq i} \{g_{k,i}^v(c_k)\}$.

S.2.3.2 Individualized Prediction

One challenge in the context of atlas discovery is to make individualized predictions when observations are predominantly limited to a single time point, i.e., when the atlas is built from cross sectional data. `LucidAtlas` provides an approach for individualized prediction based on previous observations. Note that this approach is not based on true longitudinal data (as such data is frequently not available) but instead aims to predict individual future responses based on the cross-sectional population trend.

We define our problem as follows. Given an observation y^t at x with its corresponding covariates \mathbf{c}^t at time t , how will a subject's response change when \mathbf{c}^t changes to \mathbf{c}^{t+1} at time $t + 1$?

First, we can obtain the probability distribution with `LucidAtlas`, as $p(y^t | \mathbf{c}^t, x) = \frac{1}{\sqrt{2\pi f^v(\mathbf{c}^t, x)}} \exp(-\frac{(y^t - f^m(\mathbf{c}^t, x))^2}{2 \cdot f^v(\mathbf{c}^t, x)})$.

Assumption S.2.1. We assume that the percentile of a subject remains stationary between observations at two nearby time points, i.e., the cumulative distribution, F , should be stationary: $F(y^t) = F(y^{t+1})$.

An intuitive example for the Assumption S.2.1 is that if a child has the largest airway among all 2-year-olds, it is likely that this child's airway will remain the largest over a short period of time. Now we have

$$\begin{aligned} F(y^t) &= \frac{1}{2} [1 + \operatorname{erf}(\frac{y^t - f^m(\mathbf{c}^t, x)}{\sqrt{2f^v(\mathbf{c}^t, x)}})] , \\ F(y^{t+1}) &= \frac{1}{2} [1 + \operatorname{erf}(\frac{y^{t+1} - f^m(\mathbf{c}^{t+1}, x)}{\sqrt{2f^v(\mathbf{c}^{t+1}, x)}})] . \end{aligned} \quad (\text{S.35})$$

$$\begin{aligned} F(y^t) = F(y^{t+1}) &\Rightarrow \frac{y^t - f^m(\mathbf{c}^t, x)}{\sqrt{2f^v(\mathbf{c}^t, x)}} = \frac{y^{t+1} - f^m(\mathbf{c}^{t+1}, x)}{\sqrt{2f^v(\mathbf{c}^{t+1}, x)}} \Rightarrow \\ y^{t+1} &= f^m(\mathbf{c}^{t+1}, x) + \sqrt{\frac{f^v(\mathbf{c}^{t+1}, x)}{f^v(\mathbf{c}^t, x)}} (y^t - f^m(\mathbf{c}^t, x)) . \end{aligned} \quad (\text{S.36})$$

Therefore, an approximate individualized prediction can be obtained as $y^{t+1} \approx f^m(\mathbf{c}^{t+1}, x) + \sqrt{\frac{f^v(\mathbf{c}^{t+1}, x)}{f^v(\mathbf{c}^t, x)}} (y^t - f^m(\mathbf{c}^t, x))$.

S.3 NETWORK ARCHITECTURE

Fig. S.4 shows the network architecture of the additive subnetwork f_i , which receives the anatomical location x and covariate c_i to predict the additive contribution $f_i^m(c_i, x)$ and $f_i^v(c_i, x)$ to the mean and variance for the distributional parameters $\mu(\mathbf{c}, x)$ and $\sigma^2(\mathbf{c}, x)$ respectively. Specifically, if there is prior knowledge, we use a monotonic neural network [Kitouni et al., 2023] as the backbone to predict $f_i^m(c_i, x)$; if there is no prior knowledge, we use an MLP to predict $f_i^m(c_i, x)$. Another MLP receives the $f_i^m(c_i, x)$ with c_i and x to predict the contribution $f_i^v(c_i, x)$ to the overall variance $\sigma^2(\mathbf{c}, x)$.

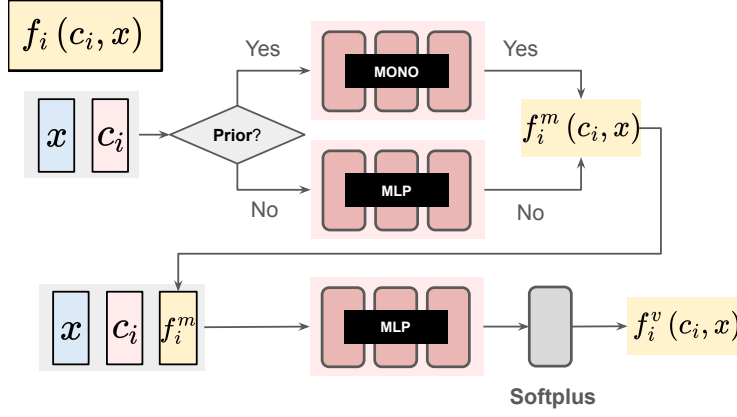


Figure S.4: Network Architecture of Additive Subnetwork f_i in LucidAtlas.

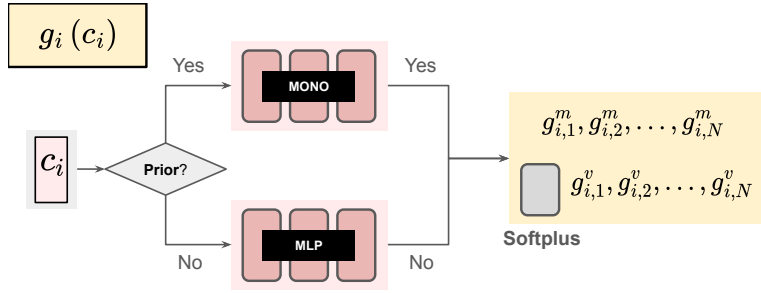


Figure S.5: Network Architecture of g_i in LucidAtlas for Modeling Covariate Dependencies.

Considering that the variance should be a number ≥ 0 , a *softplus* activation layer is used at the output of the MLP for $f_v^i(c_i, x)$ to ensure $f_v^i(c_i, x)$ is a non-negative number.

Fig. S.5 shows the network architecture for the dependence modeling network g_i , which receives the covariate c_i to predict the parameters of the conditional distributions $\{p(c_k|c_i)\}$, whose distributional parameters are $\{g_{i,k}^m\}$ for means and $\{g_{i,k}^v\}$ for variances. One can also use monotonic neural networks if prior knowledge exists about the covariate dependence. For example, for children, on average, weight increases with age. Suppose there is no prior knowledge about monotonicity. In that case, one can use Lip^1 constrained network discussed in Kitouni et al. [2023] for modeling covariates dependence, which prevents sharp and abrupt changes which are not likely to happen.

S.4 DATASETS

S.4.1 OASIS BRAIN

The Open Access Series of Imaging Studies (OASIS) is a project aimed at making MRI data sets of the brain freely available to the scientific community [Marcus et al., 2007].

The OASIS Brain dataset we use is publicly available in a preprocessed form². The OASIS Brain dataset consists of two sets, i.e.,

- 1 **A Cross-Sectional MRI Dataset (416 Subjects, Ages 18–96).** 100 of the included subjects are over the age of 60 and have been clinically diagnosed with very mild to moderate Alzheimer’s disease (AD). Additionally, a reliability data set is included containing 20 nondemented subjects imaged on a subsequent visit within 90 days of their initial session.
- 2 **A Longitudinal MRI Dataset in Nondemented and Demented Older Adults (150 Subjects, Ages 60–96).** This set consists of a longitudinal collection of 150 subjects aged 60 to 96. Each subject was scanned on two or more visits,

²<https://www.kaggle.com/datasets/jboysen/mri-and-alzheimers>

separated by at least one year for a total of 373 imaging sessions. For each subject, 3 or 4 individual T1-weighted MRI scans obtained in single scan sessions are included. The subjects are all right-handed and include both men and women. 72 of the subjects were characterized as nondemented throughout the study. 64 of the included subjects were characterized as demented at the time of their initial visits and remained so for subsequent scans, including 51 individuals with mild to moderate Alzheimer’s disease. Another 14 subjects were characterized as nondemented at the time of their initial visit and were subsequently characterized as demented at a later visit.

Our experiments include four covariates: age, socioeconomic status (SES), mini-mental state examination (MMSE), and clinical dementia rating (CDR). The outcome variable is normalized whole brain volume (nWBV), which is a scalar.

We aim to investigate the relationships between these covariates and brain volume. Based on prior knowledge, the atlas brain volume should not increase with age or CDR, nor decrease when mental state improves.

S.4.2 PEDIATRIC AIRWAY

# observations	1	2	3	4	5	6	7	9	11
# patients	230	12	6	8	3	2	1	1	1

Table S.7: Number of patients for a given number of observations for the pediatric airway dataset. For example, the 1st column indicates that there are 230 patients who were only observed once.

The airway shapes are extracted from computed tomography (CT) images. The real CT images are from children ranging in age from 1 month to ~ 19 years old. Acquiring CT images is costly. Further, CT uses ionizing radiation which should be avoided, especially in children, due to cancer risks. Hence, it is difficult to acquire such CTs for many children. Instead, the data was acquired by serendipity from children who received CTs for reasons other than airway obstructions (e.g., because they had cancer) [Jiao et al., 2023]. This also explains why it is difficult to acquire longitudinal data. E.g., one of the patients has 11 timepoints because a very sick child was scanned 11 times.

The pediatric airway dataset includes 230 cross-sectional observations (where a patient was only imaged once) and 34 longitudinal observations. 176 patients (i.e., 263 shapes) have all three covariates (age, weight, height) and 11 annotated anatomical landmarks. 6 landmarks are located on the upper airway section for this experiment. Errors in the shapes $\{\mathcal{S}^k\}$ may arise from image segmentation error, differences in head positioning, missing parts of the airway shapes due to incomplete image coverage, and dynamic airway deformations due to breathing. Table S.7 shows the distribution of the number of observations across patients. Most of the patients in the dataset only have one observation; only 22 patients have ≥ 3 observation times. Table S.8 shows the shapes and demographic information at different age percentiles for the whole data set. Similar to the OASIS Brain dataset, the time span of the longitudinal data for each patient is far shorter than the time span across the entire dataset.


P-	0	10	20	30	40	50	60	70	80	90	100
											
P-	0	10	20	30	40	50	60	70	80	90	100
age	1.00	23.00	55.00	71.00	89.00	111.00	129.00	161.00	179.00	199.00	233.00
m-vol	4.56	16.84	29.53	28.91	27.31	70.90	71.23	43.34	78.63	102.35	113.84

Table S.8: Visualization and demographic information of our 3D airway shape dataset. Shapes of $\{0, 10, 20, 30, 40, 50, 60, 70, 80, 90, 100\}$ -th age percentiles are plotted with their covariates (age/month) printed in the table. M-vol (measured volume) is the volume (cm^3) of the gold standard shapes based on the actual imaging.

Model	LucidAtlas				NAMLSS	MLP+NLL
	f_i^m or f_i^v		g_i		f_i	
	Monotonic	MLP	Monotonic	Lip^1 Constrained	MLP	
Layers	$[D_{in}, 128, D_{out}]$	$[D_{in}, 128, D_{out}]$	$[D_{in}, 128, D_{out}]$		$[D_{in}, 128, D_{out}]$	$[D_{in}, 128, D_{out}]$
Activation	GroupSort	GeLU	GroupSort		GroupSort	GeLU
Learning Rate	1e-2					
Num of Epoch	500					
Output Activation	Linear, Softplus					
Others	Adam optimizer, CosineAnnealingLR, Earlystopping					

Table S.9: Hyperparameter Settings for Comparison Methods. GroupSort and Lip^1 -constrained networks were introduced in [Kitouni et al., 2023]. Here, D_{in} represents the input dimension, while D_{out} denotes the output dimension. For details on D_{in} and D_{out} , refer to Fig. S.4 and Fig. S.5.

S.4.2.1 Data Preparation for Pediatric Airway Atlas

The image processing pipeline includes three steps: 1) automatic airway segmentation from CT images; 2) airway representation with a centerline and cross sections.

Airway Segmentation. A deep learning-based approach is used for automatic upper airway segmentation from CT images. The segmentation model is trained in two steps. The first step predicts the segmentation using a coarse version of the scans. The second step makes the segmentation prediction on original images. This step takes in the image as input, but also uses the first step prediction as an additional input. Each step is implemented as a U-Net [Özgün Çiçek et al., 2016, Ronneberger et al., 2015].

The automatic segmentation model is developed based on a dataset containing 68 pairs of airway CT images and their corresponding manual segmentations.

Centerline and Cross Sections. The pediatric airway dataset is constructed by extracting 358 airway geometries from CT images with our automatic segmentation approach. The upper airways, like any tube-like structures, can be approximated by a centerline with cross sections [Hong et al., 2013]. Following the approach in [Hong et al., 2013], the airway centerline is inferred based on the heat distribution along the airway provided by solving Laplace’s equation. The iso-surfaces of heat values are extracted from the Laplace solution and the centerlines are considered as the centers of the iso-surfaces. Cross sections are cut from the airway geometry using planes that are orthogonal to the tangent of the centerline.

Pediatric Airway Atlas Construction. Similar as the approach in [Hong et al., 2013], the cross-sectional area is considered as the airway’s main feature. For each point on the centerline, it has a distance x from the nasal spine which is normalized to 1 over the length of the airway, and a cross-sectional area y . The 1D function for airway geometry is the curve $c(x)$ that smoothly passes through all these points on the centerline, as $y = c(x)$.

The airway curves are aligned based on six key anatomic landmarks $\{\mathbf{p}_i\}$: nasal spine, choana, epiglottic tip, true vocal cord (TVC), subglottis, and carina.

Each landmark $\mathbf{p}_i = (p_{ix}, p_{iy}, p_{iz})$ is projected onto the centerline to obtain the corresponding depth x_i along the centerline. For example, the depth of nasal spine $x_{nasal\ spine}$ should be at 0 while the depth of carina x_{carina} should be at 1. For each landmark, there is a mean position $\bar{\mathbf{p}}_i = (\bar{p}_{ix}, \bar{p}_{iy}, \bar{p}_{iz})$ and the mean depth \bar{d}_i of that landmark over all cases.

A landmark-based curve registration approach [Hong et al., 2013] is used to estimate a piece-wise linear warping function $h_k(\cdot)$ for each curve $c_k(\cdot)$, which is strictly monotonic and places the landmark points for a particular subject k at the mean location of these landmarks in the atlas, $x_i = h_k(\bar{x}_i)$. With the constructed warping functions, curves can then be resampled to the normalized coordinate system with $C_k(x) = c_k(h_k(x))$.

S.5 EXPERIMENTAL SETUP

Tab. S.9 illustrates the hyperparameter settings of our approach, for NAMLSS [Thielmann et al., 2024] and the $MLP+NLL$ comparison. For our approach and all comparison methods, we use 15% of the training data set by the patient as a validation set for early stopping. The batch size for the Pediatric Airway Dataset is set to 1024, while for the OASIS Brain dataset

it is set to 32. For other comparison methods, we use their publicly available implementation, which we describe in the following.

NAM. We use the official PyTorch implementation of NAM³. We evaluate the NAM using feature networks with one hidden layers (to keep consistent with hyperparameter settings in Table. S.9), each containing 128 units and employing ExU activation. A dropout rate of 0.1 is applied, and the ensemble consists of 20 learners. We use 15% of the training data set by patient as a validation set for early stopping. All other experimental settings follow the recommended or default configurations.

Explainable Boosting Machine. The explainable boosting machine (EBM) is an open-source Python implementation⁴ of the gradient-boosting GAM that is available as a part of the InterpretML library [Lou et al., 2013, Nori et al., 2019]. We use 15% of the training data set by patient as a validation set for early stopping. We use the default hyperparameter setting, because we did not find a significant improvement when tuning the hyperparameters. EBM allows for control of the monotonicity of features by using isotonic regression. We find introducing prior knowledge improves EBM’s performance, and thus, we use the same prior knowledge for EBM as we used in our *LucidAtlas*.

LightGBM. LightGBM is a gradient boosting framework that uses tree-based learning algorithms [Ke et al., 2017]. We use the open-source implementation⁵. We use 15% of the training data set by patient as a validation set for early stopping. We find that the recommended or default configurations work well.

Hardware. The deep learning models are trained on a single NVIDIA GeForce RTX 3090 GPU and an Intel(R) Xeon(R) Gold 6226R CPU.

S.6 MORE RESULTS AND VISUALIZATIONS

Table S.10 presents the quantitative evaluation of population distribution estimation based on the Expected Calibration Error (ECE), demonstrating that incorporating prior knowledge enhances performance on the pediatric airway dataset.

Table S.11 evaluates the impact of accounting for covariate dependencies in marginalization. The results highlight that considering these dependencies is crucial for accurately interpreting the effects of individual covariates in neural additive models.

Fig.S.7, Fig.S.8 and Fig.S.9 illustrate covariate interpretations at the subglottis, epiglottic tip and nasal spine in the pediatric airway dataset. These visualizations emphasize the importance of modeling covariate dependencies when interpreting covariate effects.

Fig. S.10 compares the covariate interpretations when ignoring or using covariate dependencies. Fig.S.11 and Fig.S.12 visualize the pairwise conditional distribution $p(c_k|c_i)$ for covariates in the pediatric airway dataset and the OASIS Brain dataset, respectively.

Fig. S.6 visualizes pediatric airway CSA functions with uncertainties across different ages, incorporating marginalized covariate interpretation while accounting for covariate dependence in *LucidAtlas*. The visualization reveals that both the average airway CSA and population variance increase as children grow.

³<https://github.com/lemeln/nam/tree/main?tab=readme-ov-file>

⁴<https://github.com/interpretml/interpret/tree/3e810552f7fcae641bf6bd945f10c66bf56c424b>

⁵<https://lightgbm.readthedocs.io/en/latest/index.html>

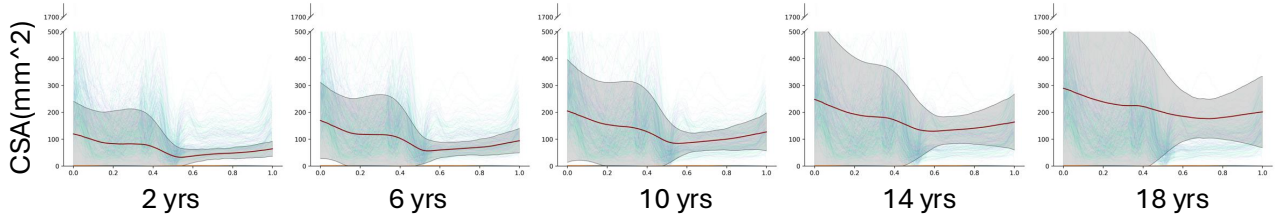


Figure S.6: Visualization of Pediatric Airway CSA Functions with Uncertainties Across Different Ages. In each subplot, the x-axis represents the normalized airway depth along the centerline (from the tip of the nose at 0 to the carina at 1), while the y-axis denotes the airway CSA at that depth. **Green** and **purple** lines indicate training and testing samples respectively. Both the average airway CSA and population variance increase as children grow.

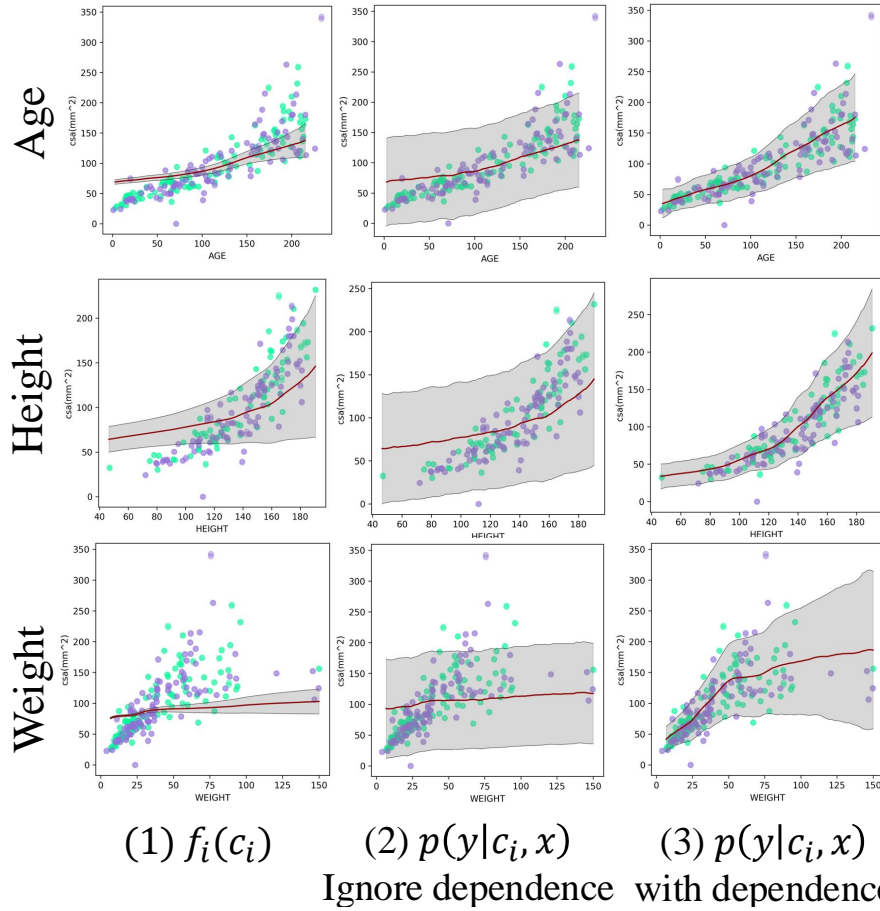


Figure S.7: Visualizations of Covariate Interpretations from LucidAtlas for CSA Distribution at the Subglottis Landmark (Pediatric Airway Dataset). (1) $f_i(c_i)$ represents the disentangled covariate effect directly from a NAM as illustrated in Sec. 3.2.2; (2) Marginalized covariate interpretation without accounting for covariate dependence; (3) Marginalized covariate interpretation incorporating covariate dependence. **Green** dots denote training samples, while **purple** dots indicate testing samples. The **red** lines represent the learned population trend, and the **gray** shading spans $\pm 2 \times$ standard deviations. Considering covariate dependence is essential for accurately capturing how each covariate influences the population trend and associated uncertainties.

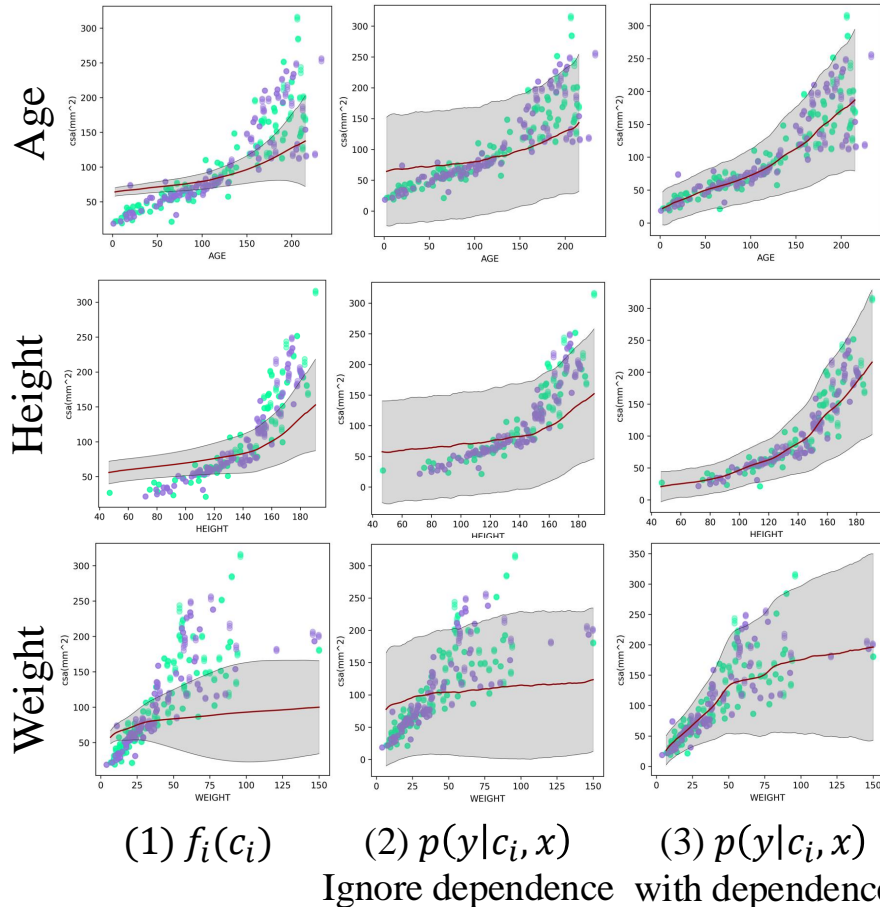


Figure S.8: Visualizations of Covariate Interpretations from LucidAtlas for CSA Distribution at the Epiglottic Tip Landmark (Pediatric Airway Dataset). (1) $f_i(c_i)$ represents the disentangled covariate effect directly from a NAM as illustrated in Sec. 3.2.2; (2) Marginalized covariate interpretation without accounting for covariate dependence; (3) Marginalized covariate interpretation incorporating covariate dependence. Green dots denote training samples, while purple dots indicate testing samples. The red lines represent the learned population trend, and the gray shading spans $\pm 2 \times$ standard deviations. Considering covariate dependence is essential for accurately capturing how each covariate influences the population trend and associated uncertainties.

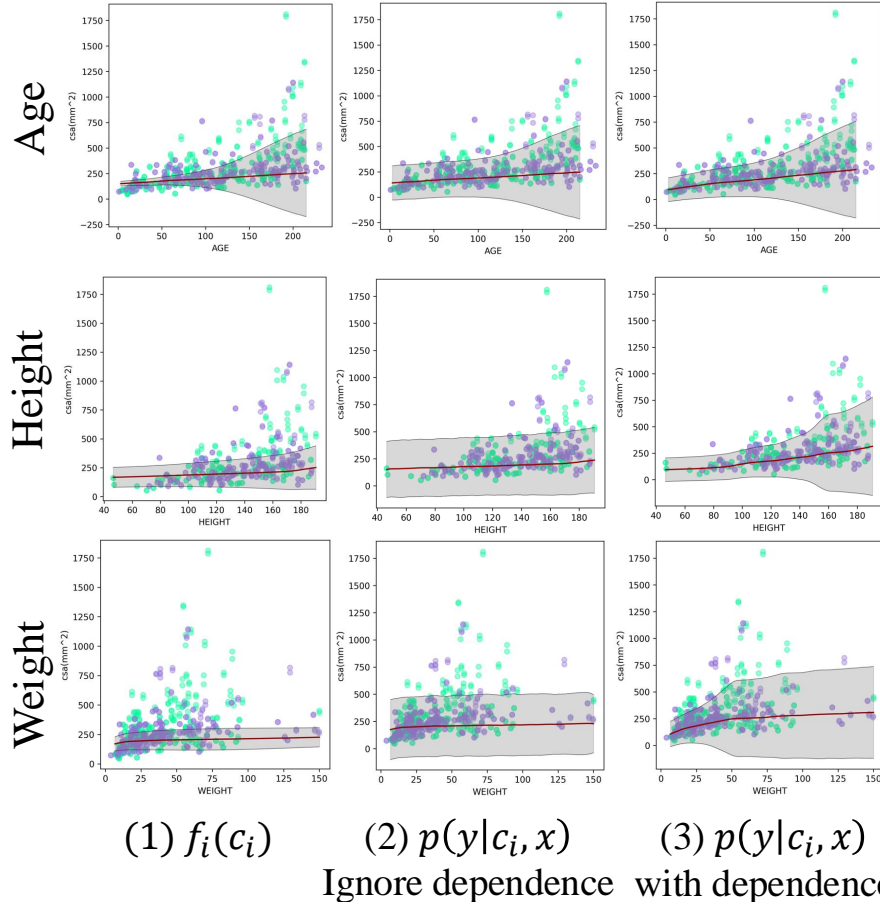


Figure S.9: Visualizations of Covariate Interpretations from LucidAtlas for CSA Distribution at the Nasal Spine Landmark (Pediatric Airway Dataset). (1) $f_i(c_i)$ represents the disentangled covariate effect directly from a NAM as illustrated in Sec. 3.2.2; (2) Marginalized covariate interpretation without accounting for covariate dependence; (3) Marginalized covariate interpretation incorporating covariate dependence. Green dots denote training samples, while purple dots indicate testing samples. The red lines represent the learned population trend, and the gray shading spans $\pm 2 \times$ standard deviations. Considering covariate dependence is essential for accurately capturing how each covariate influences the population trend and associated uncertainties.

Methods	Spa.	Add.	Mono.	OASIS Brain	Pediatric Airway						
					Overall	nasal spine	choana	epiglottic tip	TVC	subglottis	carina
MLP+NLL	✗	✗	✗	0.0150	0.0454	0.0713	0.052	0.0727	0.1023	0.1071	0.0262
NAMLSS	✗	✓	✗	0.0189	0.0572	0.116	0.0316	0.0243	0.1047	0.0949	0.158
Ours np	✓	✓	✗	0.0110	0.0400	0.0261	0.0131	0.0673	0.0686	0.0452	0.0398
Our part	✓	✓	✓	0.0161	0.0236	0.0266	0.0312	0.1177	0.0545	0.0467	0.0175
Ours imp	✓	✓	✓	0.0187	0.0248	0.0805	0.0326	0.0553	0.0732	0.0673	0.0522

Table S.10: Quantitative Evaluation of Population Distribution Estimation Using Expected Calibration Error (ECE). **Bold red values** indicate the best scores across all methods. **Bold black values** indicate the 2nd best scores of all methods. Our approach achieves the best performance overall.

OASIS Brain		
Covariate	Corr.	Overall
AGE	✗	1.0233
AGE	✓	0.9151
SES	✗	1.9071
SES	✓	1.2447
MMSE	✗	1.8732
MMSE	✓	1.0849
CDR	✗	1.8208
CDR	✓	1.0408

Table S.11: Quantitative Comparison of Different Ways of Marginalization for OASIS Brain Dataset. NLL is computed between the marginalized covariate interpretation and the data distribution. A ✓ in the **Corr.** column indicates that covariate dependence is considered, while ✗ signifies that it is ignored. Accounting for covariate dependence improves alignment between covariate interpretation and the data distribution.

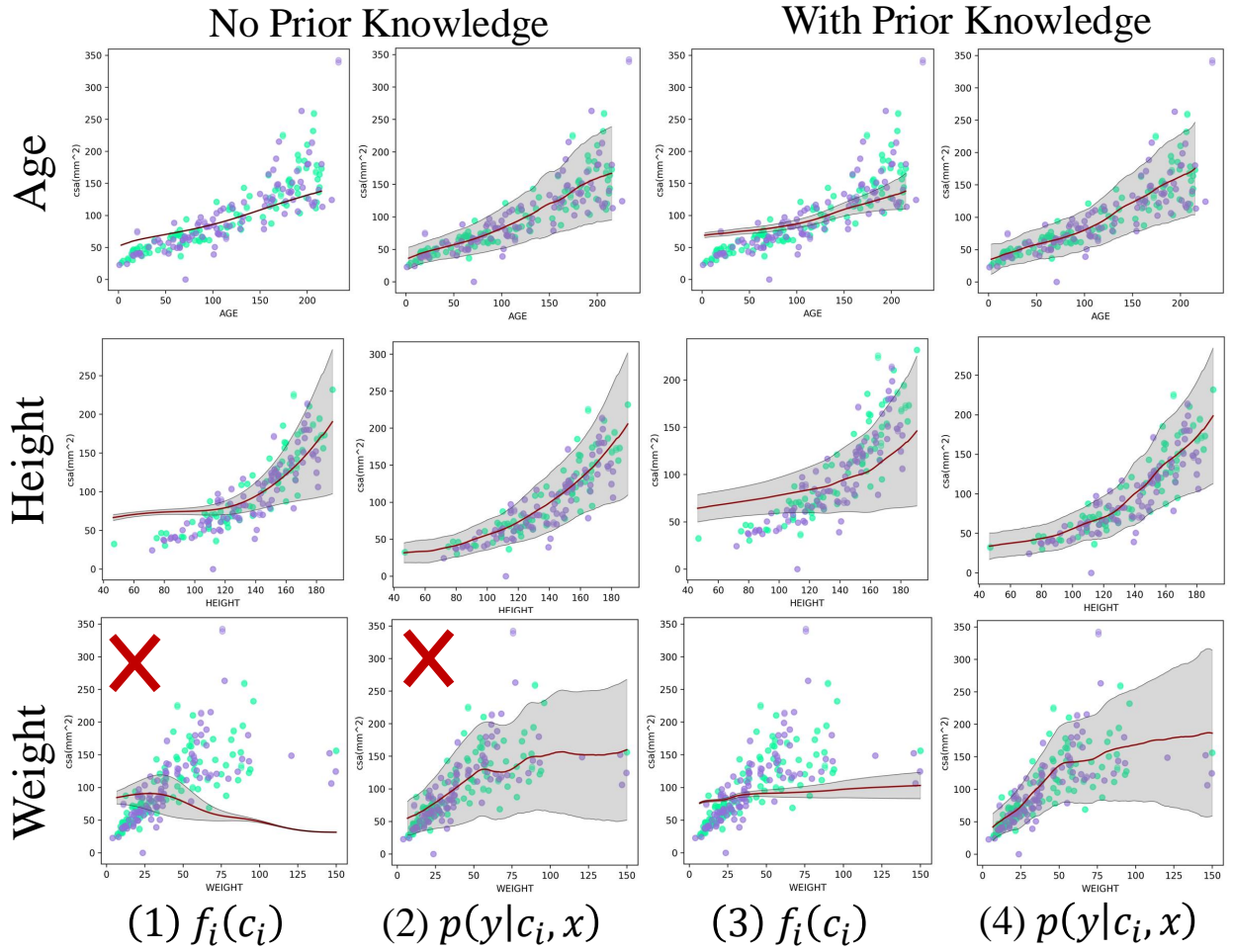


Figure S.10: Visualizations of the Effect of Prior Knowledge in *LucidAtlas* at the Subglottis Landmark (Pediatric Airway Dataset). The \times symbol indicates the covariate interpretation contradicts prior knowledge, such as the NAM incorrectly interpreting airway CSA as decreasing with a child's weight. Without incorporating prior knowledge, the model may deviate from our prior assumptions. Without marginalization, to account for covariate dependencies, the data may not be fit well.

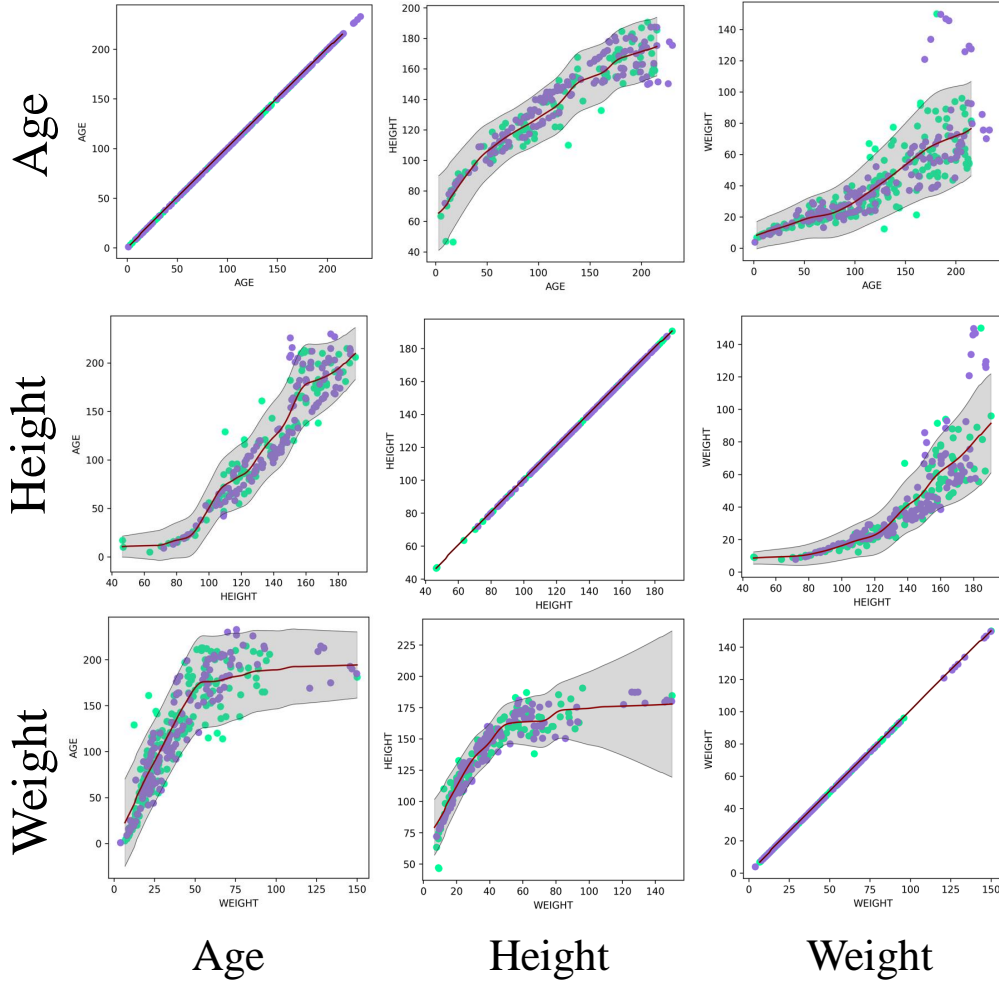


Figure S.11: Pairwise Conditional Distribution $p(c_k|c_i)$ of Age, Height and Weight in the Pediatric Airway Dataset learned by LucidAtlas.

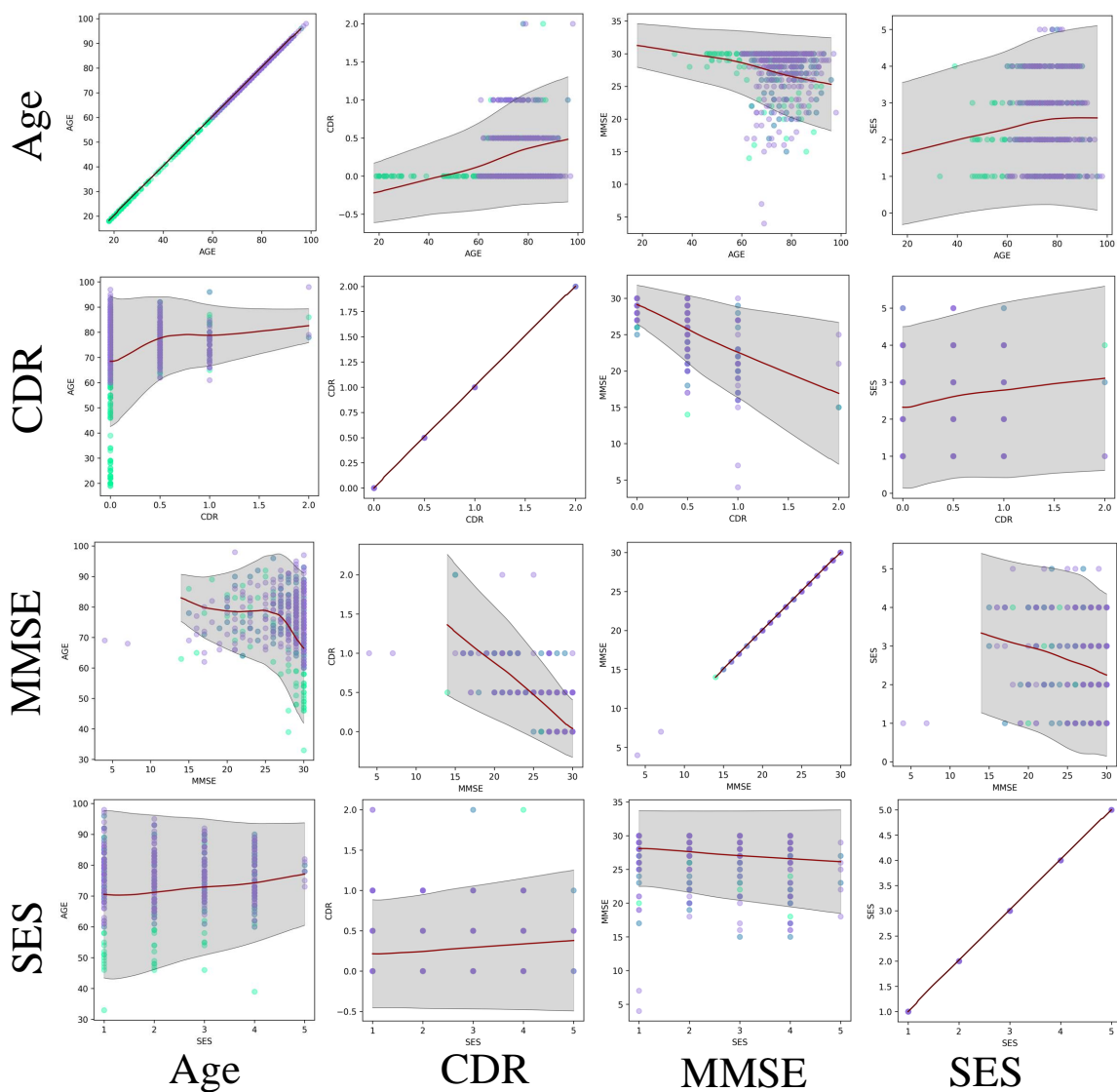


Figure S.12: Pairwise Conditional Distribution $p(c_k|c_i)$ of Age, Clinical Dementia Rating (CDR) Socioeconomic Status (SES), Mini-Mental State Examination (MMSE) in the OASIS Brain Dataset learned by LucidAtlas.